



# ATLAS NOTE

ATLAS-CONF-2014-047

July 4, 2014



## Alignment of the ATLAS Inner Detector and its Performance in 2012

The ATLAS Collaboration

### Abstract

The alignment of the ATLAS Inner Detector tracking system has been tuned using advanced procedures for the analysis of the LHC  $\sqrt{s} = 8$  TeV proton-proton collision data taken during 2012. The description of the detector geometry takes care of the relative alignment of the sensing devices and the magnetic field, momentum biases due to systematic deformations, misalignments affecting the reconstructed track parameters and time-dependent displacements occurring due to environmental changes. The procedures applied as well as the performance of the resulting alignment are presented.



# 1 Introduction

The Large Hadron Collider (LHC) [1] produces proton-proton collisions at unprecedented center-of-mass energies. The ATLAS detector [2] records the products of these collisions in order to make precise measurements of Standard Model (SM) processes as well as to search for new physics phenomena beyond the SM.

In order to reconstruct the trajectories of charged particles, ATLAS relies on the Inner Detector (ID) tracking system [3] which provides efficient, robust, and precise tracking measurements. The ID was successfully commissioned in 2008 [4], and since 2009 it has been operated with an efficiency greater than 99% during data-taking [5].

Hits recorded in individual detector elements are used to reconstruct the trajectories of charged particles inside the tracker and ultimately to estimate their kinematic parameters. The accuracy of this process is limited by the combination of: the finite resolutions of the detector elements, the knowledge of the magnetic field, the locations of the detector elements and finally the amount of material in the detector.

Misalignments of the active detector elements deteriorate the resolution of the reconstructed track, while correlated geometrical distortions can lead to systematic biases on the reconstructed track parameters. Of these biases the most important are those which affect the measured momentum and the measured impact parameter (the distance of closest approach to the primary vertex). These have been discussed in detail previously [6] and are reassessed using 2012 data in this note.

Biases on the momentum have an impact on many observables such as the invariant mass of resonances and the measurement of charge asymmetries [7]. Biases in the impact parameter affect measurements related to the beam-spot reconstruction [8], primary and secondary vertex reconstruction [9, 10],  $b$ -tagging performance [11, 12] and lifetime measurements [13, 14, 15]. Therefore, it is important to know the positions of all the ID detector elements within the detector volume as accurately as possible. The alignment procedure determines these positions and is necessary before any reliable physics measurements can be performed.

The ID has been aligned using a track-based technique [16, 17]. Any generic track-based alignment is confronted with a particular class of deformations to which fitted tracks have very low or no sensitivity. These so-called *weak modes* of alignment are collective detector deformations that transform one helical trajectory into another helical trajectory, without (or minimally) affecting the quality of the track fit, and its associated  $\chi^2$ . A number of updates have been applied to the ID alignment to correct for *weak mode* deformations. The relative rotation of the solenoidal  $B$ -field of the ID and the tracking system motivated an update of the magnetic field map used for the track reconstruction [6]. Corrections of the charge anti-symmetric momentum bias, based on the asymmetry of the measured  $E/p$  ratio for electrons and positrons as well as the charge dependent mass biases from  $Z \rightarrow \mu\mu$  decays, have been applied [6]. Time-dependent alignment corrections were introduced in 2012 to correct for movements of the ID induced by environmental changes. The 2012 alignment campaign also saw for the first time the application of explicit corrections to the transverse and longitudinal impact parameter (the distance of closest approach to the primary vertex in their respective plane).

This note is organized as follows. Section 2 provides a basic description of the ID. Section 3 is a summary of the alignment procedure. Section 4 presents the performance of 2012 alignment in terms of track-to-hit residual distributions and compares the results to those obtained from a perfectly aligned detector, using Monte Carlo simulation. The tuning of the measurement uncertainties to be used in the reconstruction is explained in Section 5. Section 6 contains a discussion of sagitta deformations and charge-symmetric momentum biases and is followed by momentum resolution studies in Section 7. Section 8 reports the biases on the reconstructed impact parameter and is complemented by the study of resulting impact parameter resolution in Section 9. Conclusions are drawn in Section 10.

## 2 The ATLAS Inner Detector

### 2.1 Components of the ID

The Inner Detector tracking system [3] was designed to provide efficient and robust track reconstruction of the products of the LHC collisions. It consists of three subdetectors: Pixel, SCT and TRT. The Pixel and SCT are silicon-based detectors, built using complementary technologies, pixels and micro-strips, respectively. The TRT is a drift chamber composed of gas-filled straws. The ID provides full  $2\pi$  coverage in the  $\phi$  direction and has coverage up to  $|\eta| \leq 2.5$  for the silicon portion of the detector while the TRT covers  $|\eta| < 2.1$  (see Sections 2.2 and 2.3 for an explanation of the ATLAS coordinate system).

All three subsystems are divided into a barrel part and two end-caps. The barrel parts consist of several cylindrical layers of sensors whilst the end-caps are composed of a series of disks or wheels of sensors. The entire tracking system is embedded in a superconducting solenoid coil which produces a 2 T axial magnetic field. Schematic views of the ID barrel and end-cap are given in Figures 1 and 2, respectively. A summary of the main characteristics, including resolution, of the three ATLAS ID subdetectors is presented in Table 1.

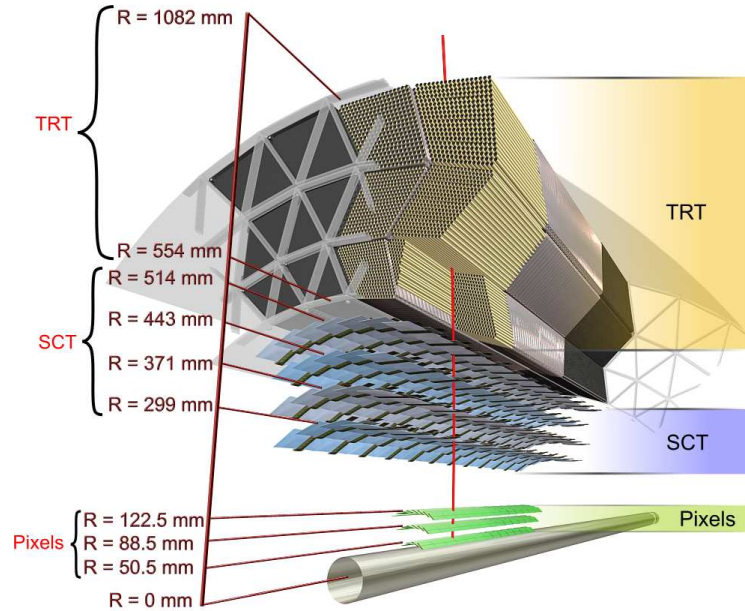


Figure 1: A diagram illustrating the sensors and structural elements in the barrel of the ID: the beryllium beam-pipe, the three cylindrical silicon Pixel layers, the four cylindrical layers of barrel silicon micro-strip modules (SCT) and 72 straw layers in the barrel transition radiation tracker (TRT) modules within their support structure.

Subdetector	Element size	Resolution [ $\mu\text{m}$ ]	Hits/track in the barrel	radius of the barrel layers [mm]
Pixel	$50\ \mu\text{m} \times 400\ \mu\text{m}$	$10 \times 115$	3	50.5, 88.5, 122.5
SCT	$80\ \mu\text{m}$	17	8	299, 371, 443, 514
TRT	4 mm	130	$\sim 30$	from 554 to 1082

Table 1: Summary of the main characteristics of the three ATLAS ID subdetectors.

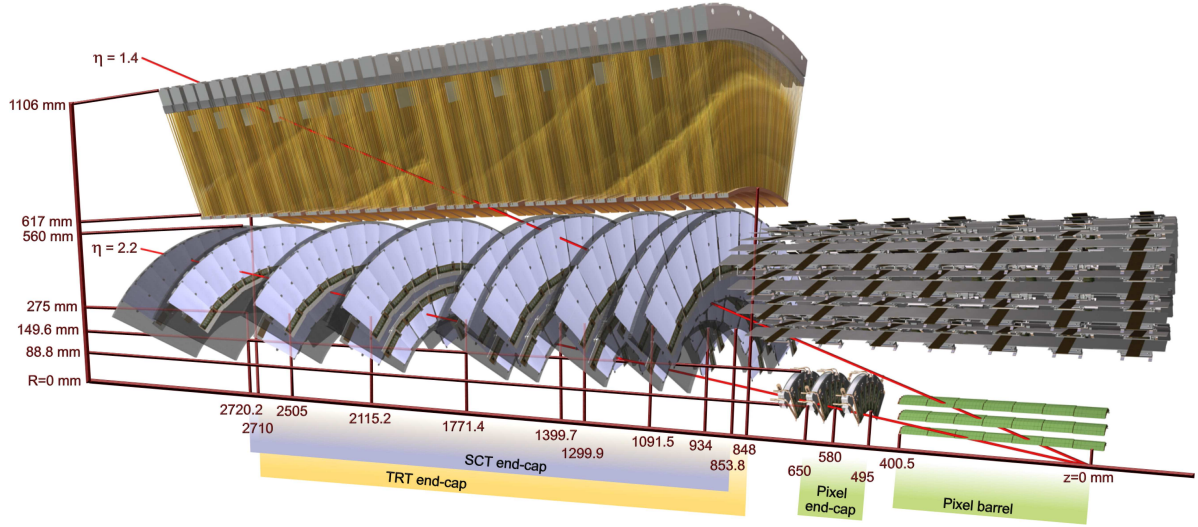


Figure 2: A diagram illustrating the sensors and structural elements in the end-cap of the ID: the beryllium beam-pipe, the three silicon-pixel disks, the nine disks of the end-cap SCT and the forty planes of TRT wheels. The Pixel and SCT barrel layers are also displayed.

## 2.2 The ATLAS coordinate system

The ATLAS coordinate system is a right-handed Cartesian coordinate system with the origin defined at the geometrical center of the detector (the nominal interaction point). The positive  $x$ -axis is defined as pointing from the interaction point to the centre of the LHC ring; the positive direction of the  $y$ -axis points upwards; and the  $z$ -axis points along the beam direction. Cylindrical coordinates  $r$  and  $\phi$  are often used in the transverse ( $x$ - $y$ ) plane.

Individual detector modules use local right-handed Cartesian reference frames with the origin in the geometrical centre of the device:

- In the Pixel and the SCT, the  $x$  and  $y$  axes are defined in the detector plane with the  $x$ -axis pointing along the most precise measurement direction. The  $x$ -axis is normally orientated along the bending or transverse plane in the ATLAS coordinate system;
- In the TRT modules and straws the  $z$ -axis points along the wire and the  $x$ -axis is perpendicular to both the wire and radial direction defined from the origin of the global frame to the straw centre.

## 2.3 Track parametrisation

The helical trajectories of tracks are parameterised in the following way [18]:

$$\tau = (d_0, z_0, \phi_0, \theta, q/p). \quad (1)$$

The transverse impact parameter ( $d_0$ ) is defined as the distance of closest approach in the transverse plane of the track to the primary vertex, while the longitudinal impact parameter ( $z_0$ ) is the  $z$  coordinate of the perigee point.  $\phi_0$  is the azimuthal angle of the track at the perigee, and  $\theta$  is its polar angle. The ratio  $q/p$  is the inverse of the particle momentum ( $p$ ) multiplied by its charge ( $q$ ). The transverse momentum,  $p_T$ , is computed as  $p_T = p \sin \theta$ . The particle pseudorapidity  $\eta$  is defined as:  $\eta = -\ln \tan(\theta/2)$ .

## 2.4 Track parameter estimation

The hits (detector measurements) left in the detector by charged particles traversing active detector elements are used to reconstruct their trajectories by performing a fit to the kinematic parameters. The track fitting is based on the minimization of the track-hit residuals:

$$\mathbf{r} = \mathbf{m} - \mathbf{e}, \quad (2)$$

where  $\mathbf{r}$  represents the residual vector of the measurements of a track,  $\mathbf{m}$  is the vector of measurements of this track in the different sensors and  $\mathbf{e}$  is the vector of their expected values according to the test track parameters  $\boldsymbol{\tau}$ .

The track fitting consists of finding the set of track parameters which minimizes the following  $\chi^2$ :

$$\chi^2 = \mathbf{r}^T V^{-1} \mathbf{r} \quad (3)$$

where  $V$  is the covariance matrix of the detector measurements [19].

## 3 Inner Detector Alignment

The Inner Detector is composed of a large number of active detector modules. The positions of these modules must be precisely known in order to fully benefit from the measurement accuracy of the tracking system. The procedure of determining these positions is known as alignment. Each module can be treated as an alignable structure and if treated as a rigid body, has six DoF that uniquely define its position and orientation in space. These six degrees of freedom (DoF) are normally decomposed into three translations ( $T_x$ ,  $T_y$ ,  $T_z$ ) of the centre of the object and three rotations ( $R_x$ ,  $R_y$ ,  $R_z$ ) around the Cartesian axes and will be referred to as the alignment parameters.

### 3.1 Method

The alignment of the ID is performed using a track-based technique which minimizes the track-to-hit residuals by correcting the alignment parameters. In the limit of small corrections the problem can be linearised and the corrections to alignment parameters ( $\mathbf{a}$ ) are obtained by solving the system of linear equations:

$$\delta \mathbf{a} = -\mathcal{M}_a^{-1} \mathbf{v}_a \quad (4)$$

where the alignment matrix and vector are defined as:

$$\mathcal{M}_a = \sum_{tracks} \left( \frac{d\mathbf{r}}{d\mathbf{a}} \right)^T V^{-1} \left( \frac{d\mathbf{r}}{d\mathbf{a}} \right) \quad \text{and} \quad \mathbf{v}_a = \sum_{tracks} \left( \frac{d\mathbf{r}}{d\mathbf{a}} \right)^T V^{-1} \mathbf{r}_0 \quad (5)$$

where  $\mathbf{r}_0$  is the vector of the original residuals [20]. This method takes all correlations between the alignable structures into account and is known as the global  $\chi^2$  method [21, 22].

The global  $\chi^2$  method requires solving a set of linear equations that is of the same size as the number of DoFs being solved for. There is a practical limit to the size of the problem that can be handled and accurately solved [23]. For very large systems, the problem can be reduced to many small linear systems by ignoring the correlations between alignable structures. Each structure is then aligned with respect to its neighbouring modules which is referred to as the local  $\chi^2$  method [17]. The disadvantage of this method is that to account for the correlations between the alignable structures many iterations need to be performed.

The alignment is performed at three different hierarchical levels (see Table 2 for details). At *Level 1* the seven largest physical structures are aligned, the Pixel sub-detector as a whole, the SCT barrel, the

two SCT end-caps and finally the TRT barrel and the two TRT end-caps. The *Level 2* alignment treats silicon barrel layers and end-cap disks and the TRT barrel modules end-cap wheels as separate objects. Finally *Level 3* aligns all silicon modules (Pixel, SCT) and the individual wires of the TRT. Depending on the alignment level, some of DoFs may be fixed during the alignment procedure (see Table 2). For the ID, this means that the Pixel, SCT and TRT modules have close to 36,000 DoF. For the TRT wire alignment, only two degrees of freedom per wire are considered ( $T_x$  and  $R_y$ ), resulting in over 700,000 DoF to be determined.

During the track-based alignment, all alignable structures are treated as rigid bodies, however, corrections have been applied to the Pixel modules to take into account the non-planarity of the modules. The corrections to Pixel modules have been determined using survey data taken during the construction of the Pixel detector [24] and are not subject to alignment corrections.

The alignment algorithms use as input a large sample of good quality tracks, recorded during proton-proton collisions produced by the LHC. The tracks used were required to have transverse momentum of at least 10 GeV, pass through at least 9 silicon measurement planes, have at least 7 silicon hits and are required to be isolated from other tracks within a cone of  $\Delta R = 0.3$ <sup>1</sup>.

### 3.2 Constraints

In order to remove *weak modes* from the alignment solution, it is necessary to propagate appropriate constraints through the alignment algorithms. Different constraints are considered depending on the expected misalignment and on the sensitivity of specific DoF for each alignable structure. Constraints can be applied to either the reconstructed parameters of the tracks used as input to the alignment algorithm or to the alignment parameters themselves [20]. Additionally, each subsystem can be aligned at any required level independently from the others. The catalog of constraints and the modularity of the algorithms allow for a variety of alignment set-ups in order to tackle different misalignments and extract accurate corrections to module positions.

The different alignment set-ups used during the 2012 campaign and their respective constraints are summarized in Table 2. All but the TRT *Level 3* (which used the local  $\chi^2$ ) used the global  $\chi^2$  method to solve for the alignment corrections.

### 3.3 Time Dependence

Starting from a fixed set of reference constants (see Section 3.4) a *Level 1* alignment is performed for each ATLAS run prior to data reconstruction to determine if the detector has moved significantly between runs. The results obtained are monitored and if a significant displacement is observed the detector alignment is corrected prior to the bulk data processing (reconstruction of the full dataset).

For example, Figure 3 displays the  $T_x$  corrections for each detector sub-system during 2012 with respect to the baseline alignment constants (see Sec. 3.4). By convention, the alignment corrections are defined relative to the Pixel detector, hence corrections for the latter are not displayed. This is not, by any means, to suggest which subsystem was physically moving. The reference alignment period used to determine the baseline constants is marked by the two vertical lines. Changes to the environmental conditions of the detector (temperature, magnetic field strength, etc.) occurring during breaks in data-taking often lead to significant movements of the detector. In addition to these relatively large movements of the detector (caused by sudden conditions changes), slow gradual drifts of the subdetectors were observed. These subtle gradual movements were attributed to mechanical relaxations after a sudden change and could take many weeks to stabilize.

The importance of correcting for the time dependence is discussed in Section 6.1.

---

<sup>1</sup>The isolation cone,  $\Delta R$ , is defined as  $\sqrt{\Delta\phi^2 + \Delta\eta^2}$ .

Level	Description	Structures	DoF	Constraints
1	Pixel detector kept fixed			
	SCT split into barrel and 2 end-caps	3	All	
	TRT split into barrel and 2 end-caps	3	All except $T_z$	
2	Pixel barrel split into layers	3	All	
	Pixel end-caps split into disks	6	$T_x, T_y, R_z$	Beam spot,
	SCT barrel split into layers	4	All	Momentum bias and
	SCT end-caps split into disks	18	$T_x, T_y, R_z$	Impact parameter bias
	TRT split into barrel and 2 end-caps	3	All except $T_z$	
Si 3	Pixel barrel modules	1456	All	
	Pixel end-caps modules	288	$T_x, T_y, R_z$	Beam spot,
	SCT barrel modules	2112	All	Momentum bias and
	SCT end-caps modules	1976	$T_x, T_y, R_z$	Impact parameter bias
	TRT barrel split into barrel modules	96	$T_x, R_z$	Module placement accuracy
	TRT end-caps split into wheels	80	$T_x, T_y, R_z$	
TRT 3	Pixel and SCT are fixed			
	TRT straw level	351k	$T_x, R_z$	

Table 2: Alignment configurations used throughout 2012.

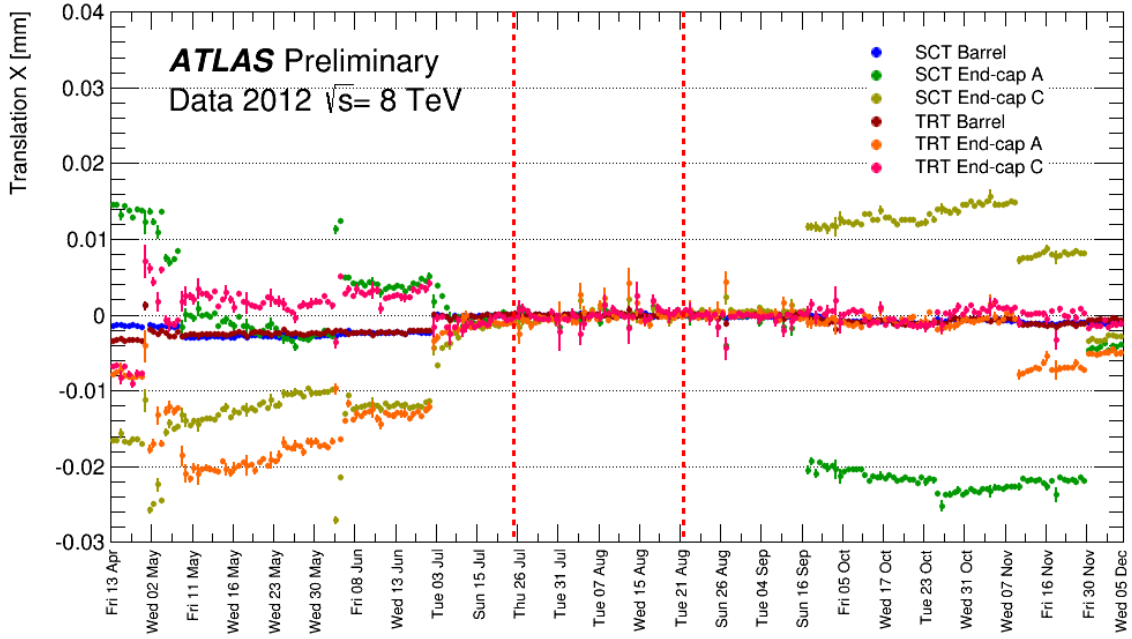


Figure 3: The corrections to the global  $X$  position ( $T_x$ ) of all ID sub-detectors with respect to the Pixel detector during 2012. The vertical dashed lines indicate the data-taking periods in which the baseline constants were determined. Errors show are statistical uncertainties on determined alignment parameter and crucially depend on the statistics of data recorded in a given run.

### 3.4 Baseline Alignment Constants

The set of alignment constants used as the basis for all subsequent alignment refinements was obtained using a large amount of data (over  $4 \text{ fb}^{-1}$ ) collected during a period of time during which the detector conditions were stable (specifically 30 runs recorded from July 22<sup>nd</sup> to August 24<sup>th</sup> 2012). This allowed for an accurate determination of alignment constants and minimization of track parameter biases (impact parameter and sagitta) due to alignment, see [6] for details of the procedures applied. All levels of alignment were performed within this stable period. To reach convergence typically two iterations at *Level 1* and three iterations at *Level 2* were required for the entire ID. At *Level 3* five iterations were required for the silicon portion while for the TRT where the local  $\chi^2$  method is used more than 30 iterations were required to take into account correlations among straws.

## 4 Track-Hit Residuals

The minimization of the track-to-hit residuals is the cornerstone of the track-based alignment. Consequently, the track-to-hit residuals are useful quantities to measure the performance of the alignment procedures. In this section residuals in data are compared to those obtained from Monte Carlo (MC) simulation using a perfectly aligned detector geometry. For the purpose of performance studies, all hits from each detector module are removed from the track fit prior to constructing track-to-hit residuals for the module under test. Residuals defined this way are referred to as *unbiased*. Tracks used for these studies originate from muons from  $Z$  boson decays. Muons have been chosen to reduce the impact of multiple scattering allowing the effects of misalignment to be clearly seen in the residual distributions.

The datasets used for studying alignment performance are statistically independent from those used for the determination of the alignment constants.

### 4.1 Data Selection

Tracks originating from  $Z \rightarrow \mu^+\mu^-$  decays are used for a number of studies throughout this note. The  $Z$  boson candidates are reconstructed from data or  $Z \rightarrow \mu^+\mu^-$  Monte Carlo simulation generated using PYTHIA [25]. The  $Z \rightarrow \mu^+\mu^-$  decays are reconstructed using pairs of oppositely charged muons each with transverse momentum of at least 25 GeV and  $|\eta| \leq 2.5$  in events triggered by either a single high- $p_T$  muon trigger or a lower- $p_T$  dimuon trigger [26].

Each muon candidate is required to be a *combined muon*: track reconstruction is performed independently in the ID and muon spectrometer (MS), and the muon candidates track is formed from the successful combination of a MS and an ID track. The muon impact parameter with respect to the primary vertex in the transverse plane or along the beam axis is required to be less than 0.2 and 1.0) mm, respectively.

In addition, all muon tracks are required to have:

- At least one hit in the first layer of the Pixel detector, if one is to be expected;
- At least one Pixel hit and five SCT hits;
- At most two Pixel or SCT holes<sup>2</sup>;
- If  $0.1 < |\eta| < 1.9$ : at least six TRT hits, including TRT outliers<sup>3</sup>, with the fraction of outlier hits being less than 0.9;

---

<sup>2</sup>A hole is defined as a missing hit in a detector sensor where a signal is expected.

<sup>3</sup>An outlier is defined as a hit discrepant from the trajectory hypothesis by more than a certain number of standard deviations (tunable within the track reconstruction algorithm).



- If  $|\eta| \leq 0.1$  or  $|\eta| \geq 1.9$ : if the track has at least six TRT hits, including TRT outliers, the fraction of TRT outliers has to be less than 0.9.

Tracks originating from  $J/\psi \rightarrow \mu^+\mu^-$  decays are also used in the studies. They are reconstructed using pairs of oppositely charged muons each with transverse momentum of at least 7.5 GeV. Events are selected with a trigger that requires two muon with  $p_T$  greater than 6 GeV. Muon tracks must satisfy the same quality criteria as used for the  $Z \rightarrow \mu^+\mu^-$  selection.

Identical event reconstruction and track selection requirements are applied to both MC and data samples. Where appropriate, the MC has been normalized to the number of entries in the data distributions.

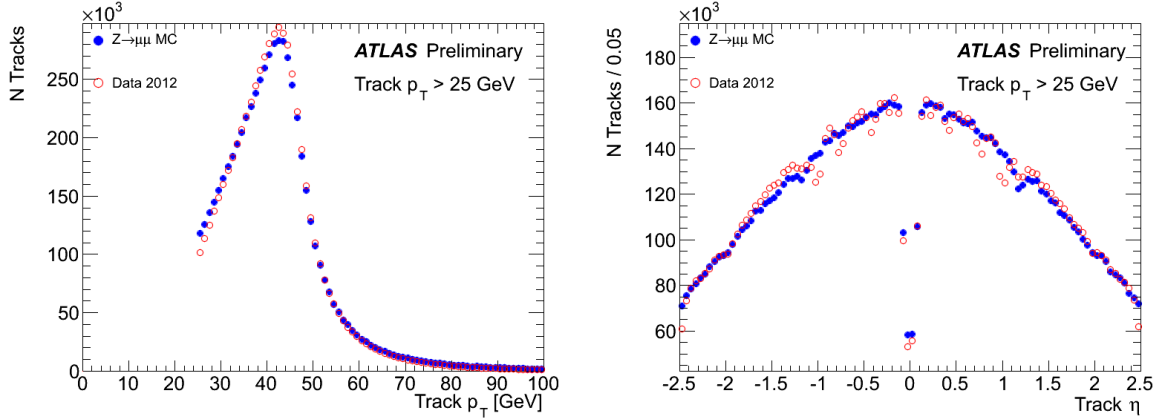


Figure 4: Muon track  $p_T$  and  $\eta$  distributions in the selected  $Z \rightarrow \mu^+\mu^-$  data and MC simulation samples. Contribution of background to the  $Z \rightarrow \mu^+\mu^-$  peak in data is small and has been neglected.

Many of the observables are track- $p_T$  and  $\eta$  dependent. For example, due to the impact of multiple scattering the width of hit-on-track residual distributions depends strongly on the  $p_T$  spectra of the tracks, and on the  $\eta$  distribution, due to the variable intrinsic resolutions of ID modules traversed by the tracks at different incident angles. Therefore, in order to draw meaningful conclusions about the ID alignment performance, it must be ensured that the kinematics of data and MC are in reasonable agreement. This is shown in Figure 4. The ratio of Data to MC does not deviate from unity more than 15% and 5% in  $p_T$  and  $\eta$ , respectively.

## 4.2 Track-hit residual in $Z \rightarrow \mu^+\mu^-$ events

Figure 5 shows the local  $x$  residual distribution for all hits on tracks in Pixel barrel modules (left), and Pixel end-cap modules (right). Similarly, Figure 6 shows the local  $y$  residual distributions (the projection of the residual onto the module local  $y$  direction) for Pixel barrel and end-cap modules, while Figure 7 shows the local  $x$  residual distribution for SCT barrel and end-cap modules. Figure 8 shows the residual distributions for TRT barrel and end-caps. Reasonably good agreement is seen between data and MC in the residual distributions of the Pixel end-caps, SCT and the TRT. In the case of the Pixel barrel larger residual widths are observed in the data. The effect is quantified on the plots in terms of the Full Width Half Maximum (FWHM) figures of merit. Possible causes for the data-MC disagreement are discussed in Section 4.5.

## 4.3 Average Silicon Residuals

The averages of the residual distributions for each module or layer provide another powerful tool to quantify possible misalignments. The quantity allows for misalignment effects to be disentangled from

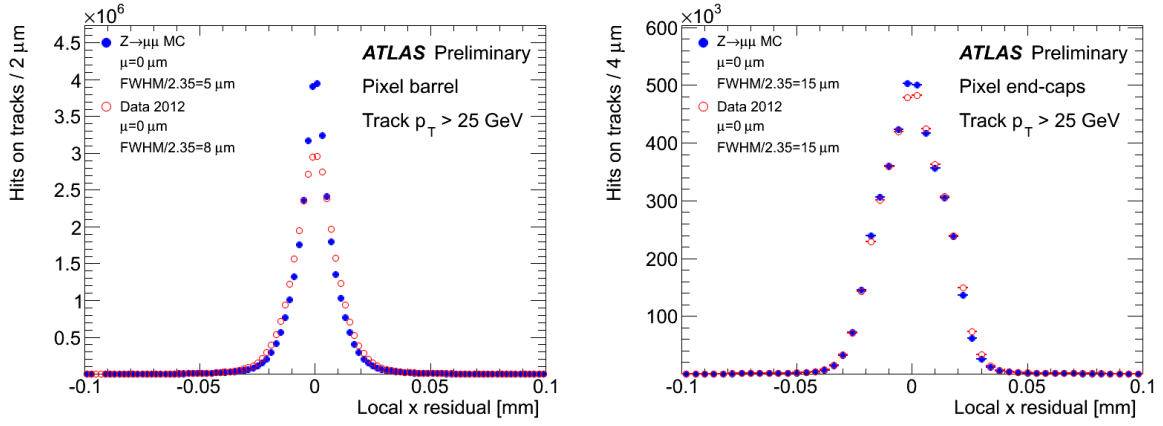


Figure 5: The Pixel local  $x$  residual distributions for the  $Z \rightarrow \mu^+\mu^-$  data sample reconstructed with the 2012 Alignment constants (open circles), compared with the  $Z \rightarrow \mu^+\mu^-$  MC simulation sample (full circles). The distributions are integrated over all hits-on-tracks in barrel modules (left) and end-cap modules (right).

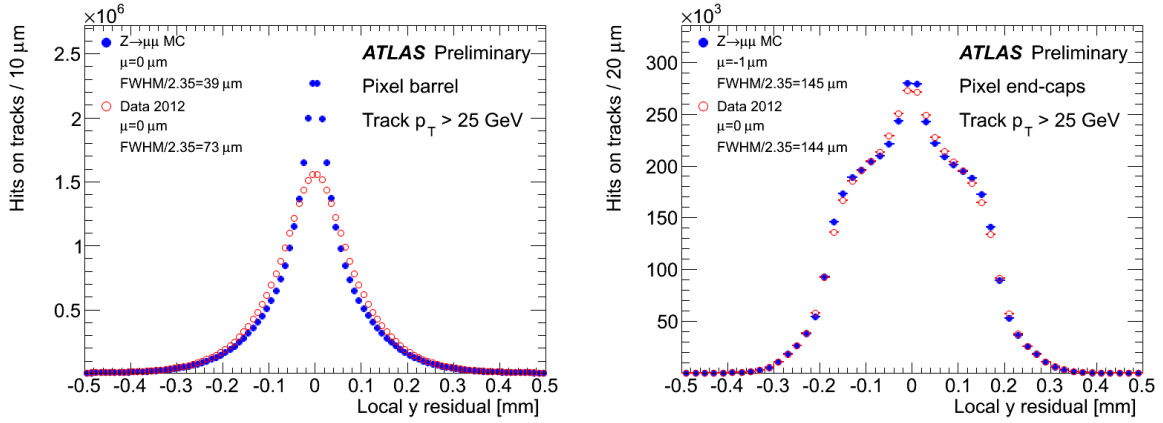


Figure 6: The Pixel local  $y$  residual distributions for the  $Z \rightarrow \mu^+\mu^-$  data sample reconstructed with the 2012 Alignment constants (open circles), compared with the  $Z \rightarrow \mu^+\mu^-$  MC simulation sample (full circles). The distributions are integrated over all hits-on-tracks in barrel modules (left) and end-cap modules (right).

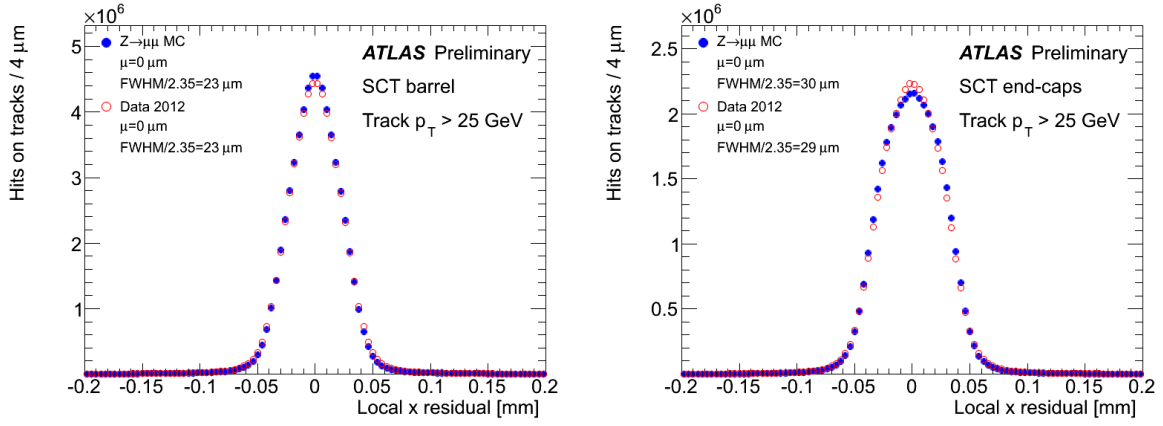


Figure 7: The SCT local  $x$  residual distributions for the  $Z \rightarrow \mu^+\mu^-$  data sample reconstructed with the 2012 Alignment constants (full circles), compared with the  $Z \rightarrow \mu^+\mu^-$  MC simulation sample (open circles). The distributions are integrated over all hits-on-tracks in barrel modules (left) and end-cap modules (right).

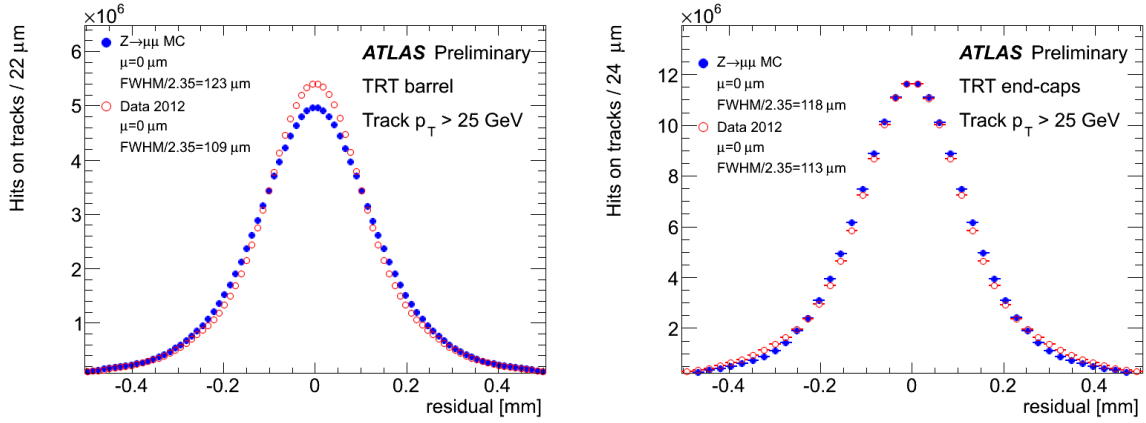


Figure 8: The TRT local  $x$  residual distributions for the  $Z \rightarrow \mu^+\mu^-$  data sample reconstructed with the 2012 Alignment constants (open circles), compared with the  $Z \rightarrow \mu^+\mu^-$  MC simulation sample (full circles). The distributions are integrated over all hits-on-tracks in barrel modules (left) and end-cap modules (right).

other effects like intrinsic resolution modeling. If a layer in the barrel or a disk in the end-caps is misaligned with respect to the other layers, the hits in the misaligned layer or disk will be systematically displaced from their ideal position, and the mean of the residual distribution for that layer or disk will be different from zero.

Figure 9 shows the average residual for each layer of the silicon detector. No deviations greater than  $0.5 \mu\text{m}$  are observed in the mean of the residual distributions as a function of the module layer in the Pixel and SCT barrels, and as a function of the module disk in the Pixel and SCT end-caps. The median values of the residual distributions for each module in each sub-detector (Figure 10) indicate, from the widths of the distributions, that the silicon modules are aligned with an accuracy of  $\sim 1 \mu\text{m}$ .

#### 4.4 Average TRT Residuals

Figure 11 shows the mean of the TRT residual distributions as a function of  $\phi$  sector for the three TRT barrel layers, and Figure 12 shows the residual mean as a function of the TRT end-cap wheel. Both in the barrel layers and end-cap wheels of the TRT, the biases are below  $1 \mu\text{m}$  and thus very small when compared with the larger intrinsic hit resolution of the TRT which is approximately  $130 \mu\text{m}$ .

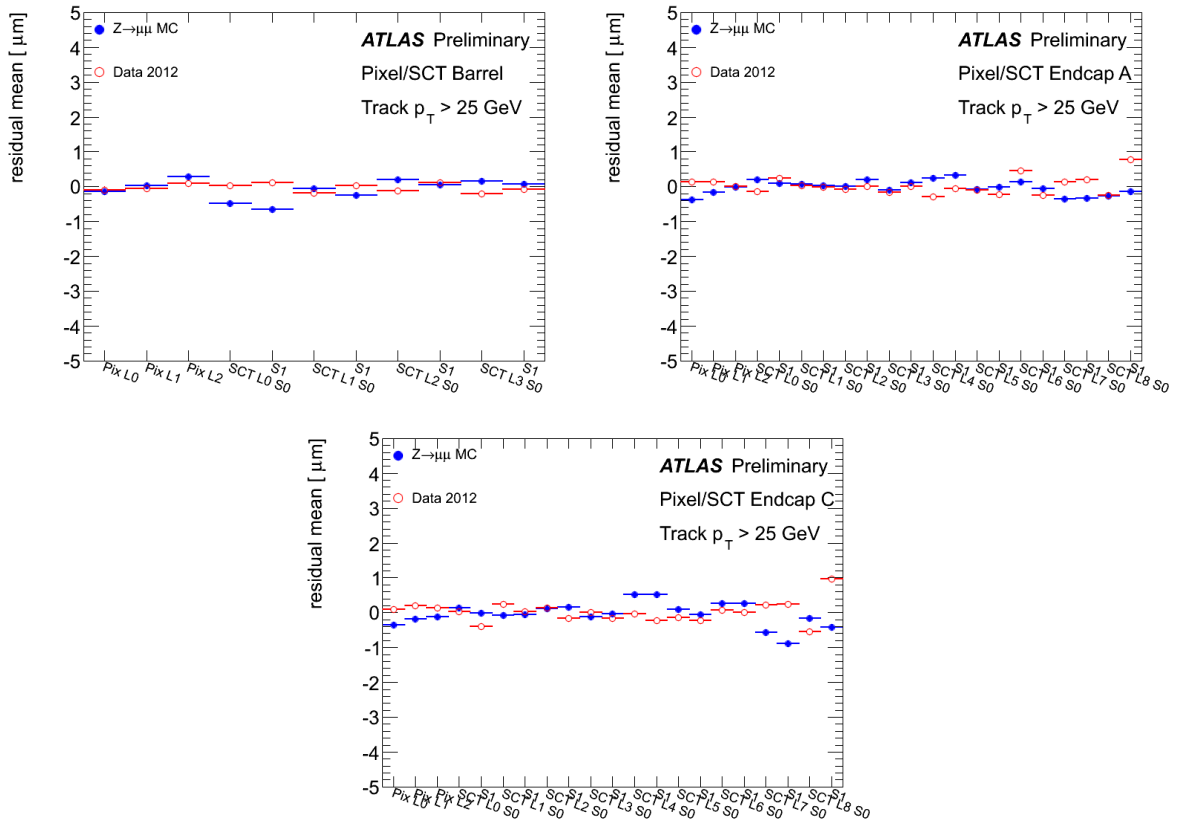


Figure 9: Mean of the residual distributions as a function of the module layer in the Pixel and SCT barrels (for SCT the sensor sides are denoted with S0 and S1), and as a function of the module disk in the Pixel and SCT end-caps. The residual distributions for the  $Z \rightarrow \mu^+\mu^-$  data sample reconstructed with the 2012 Alignment (open circles), compared with the  $Z \rightarrow \mu^+\mu^-$  MC simulation sample (full circles).

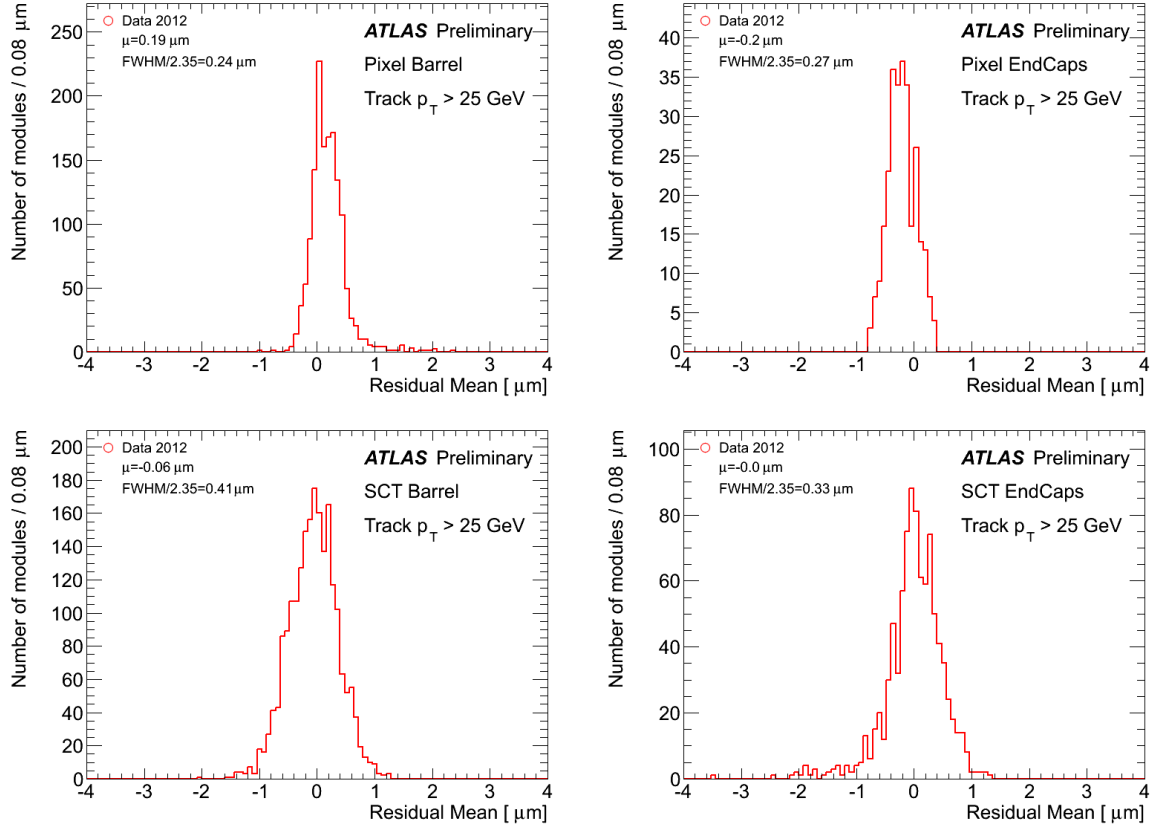


Figure 10: Median of the residual distribution for each module in the Pixel and SCT barrel, and for the Pixel and SCT end-caps. The median residual distributions were created using tracks from  $Z \rightarrow \mu^+\mu^-$  decays reconstructed with the 2012 Alignment constants. Reported on the plots are means of the distribution,  $\mu$ , and  $\text{FWHM}/2.35$  which approximate one standard deviation.

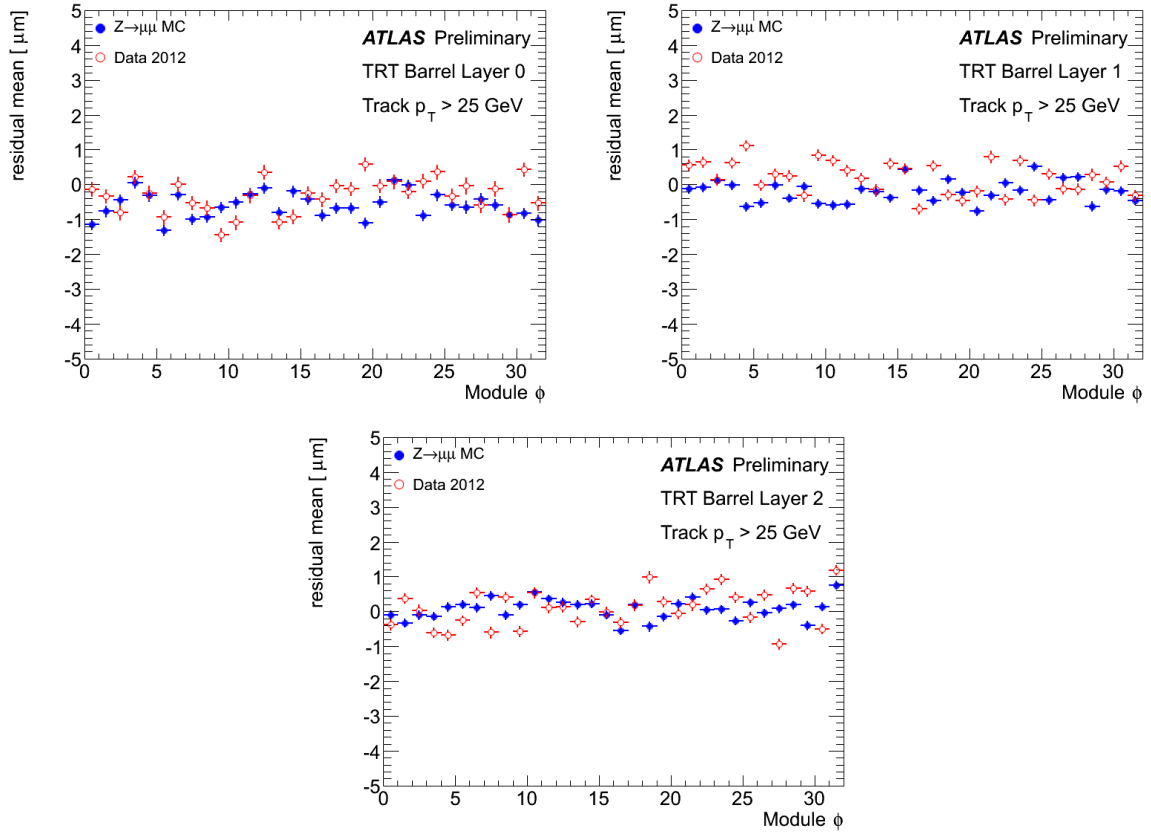


Figure 11: Mean of the residual distributions as a function of  $\phi$  sector for the three layers of the TRT barrel. The residual distributions for the  $Z \rightarrow \mu^+\mu^-$  data sample reconstructed with the 2012 Alignment (open circles) are compared with the  $Z \rightarrow \mu^+\mu^-$  MC simulation sample (full circles).

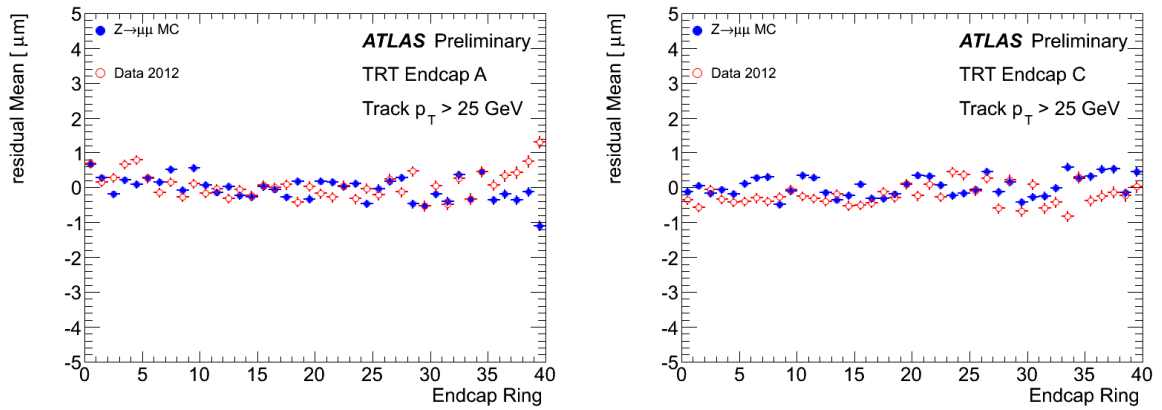


Figure 12: Mean of the residual distributions as a function of end-cap wheel in the TRT end-cap A and end-cap C. The residual distributions for the  $Z \rightarrow \mu^+\mu^-$  data sample reconstructed with the 2012 Alignment (open circles) are compared with the  $Z \rightarrow \mu^+\mu^-$  MC simulation sample (full circles).

## 4.5 Data-MC Discrepancies

The largest data-MC simulation disagreement observed in the residual studies was in the inclusive residual distributions of the Pixel barrel modules. The inclusive residual discrepancies, if alignment was the sole cause, indicate a misalignment on the order of  $6\ \mu\text{m}$  after subtracting the resolution seen in MC simulation. This, however, contradicts the observed mean values of residuals in the Pixel modules which indicate the modules are aligned at  $1\ \mu\text{m}$  level.

Studies to understand the actual mechanism are underway. Various possible causes of the observed discrepancy between data and MC have been considered, e.g.:

- imperfect modeling of the material interaction in the MC simulation,
- detector movements that occur with a frequency greater than once per hour,
- residual biases not uniform across individual modules,
- mis-modeling of the detector response (and resolution) in the simulation.

For example, the assumption that the MC simulation perfectly models the detector response is known to be incorrect for both the SCT and Pixel detectors where the cluster size in MC simulation is underestimated (see Figure 13). This is a possible factor contributing to the resolution of the detector being better in MC simulation than in data. However, given the cluster size is approximately 5% larger in data than simulation, it seems unlikely to be the only cause of the discrepancy in the residual width which is approximately 100% larger in data than in simulation.

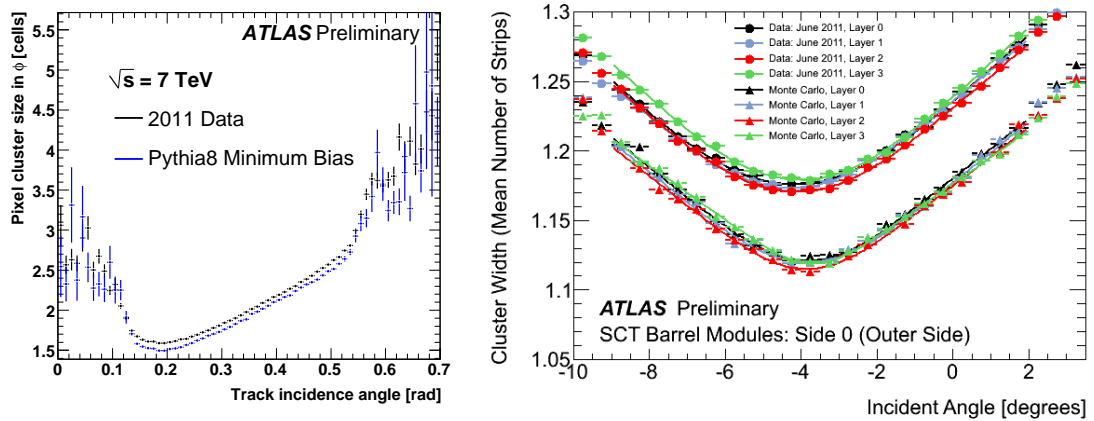


Figure 13: The mean cluster size as a function of the incidence angle for the Pixel detector (left) [27] and the SCT barrel (right) [28]. Distributions for both data and Monte Carlo simulation are shown.

## 5 Error Scaling

### 5.1 Description

Error scaling is an iterative procedure for correcting the measurement uncertainties of the ID components. It is neither determined nor directly used in the alignment procedure itself. Error scaling determination is performed post-alignment and used in the reconstruction, at the same time providing useful information about the resultant detector resolution. If the intrinsic resolution, ( $\sigma_0$ ), of each detector was truly representative of the uncertainty on a hit position, the track-to-hit pull distributions would be Gaussian with

a mean of zero and a standard deviation of one. Due to module misalignments and other effects that are not corrected for, the pull distributions in data typically have a standard deviation greater than one. The approach for correcting this is to fit a Gaussian function to the pull distribution, extract the width, apply a small correction to the uncertainty based on the fitted width, and recalculate the pull distributions. This procedure is repeated until the pull width converges to one. A Gaussian function is used for all measurements in order to emulate how the measurement will be treated in the track fit<sup>4</sup>. The hit uncertainty is parameterised as

$$\sigma = \sigma_0 \oplus C \quad (6)$$

The second term in the quadrature sum,  $C$ , is the error scaling term that accounts for module misalignments and any other effects that result in uncertainties deviating from  $\sigma_0$ . The error scale is determined for each detector type and degree of freedom, separately for barrel and end-cap, yielding a total of eight error scale parameters. The procedure itself is independent from alignment and is performed after a new set of alignment constants have been determined.

## 5.2 Results for 2012 data

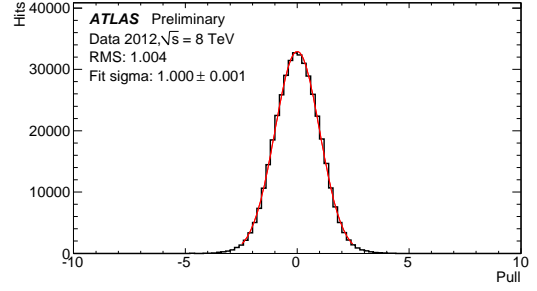
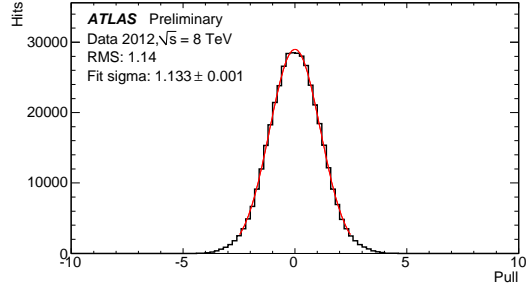
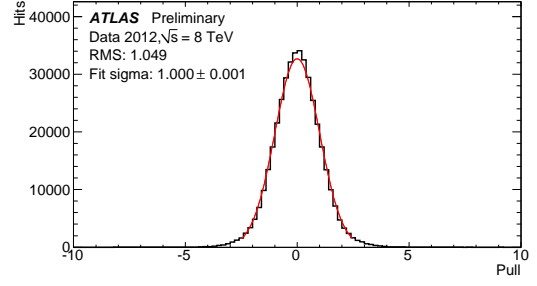
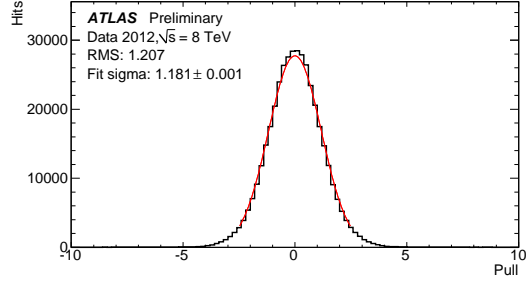
Error scaling parameters are determined using a sample of about  $10^5$  tracks taken from proton-proton collision with  $p_T > 10$  GeV with at least 9 hits in the silicon detectors and no holes in the Pixel detector. The uncorrected pull distributions of the Pixel barrel and end-cap residuals are shown in Figures 14(a) and 14(c), respectively. The non-Gaussian shape of the local  $y$  pulls in the end-caps is caused by a large fraction of single-pixel clusters in this region. Still, the Gaussian fit to the distributions was used throughout as this best represents the Gaussian uncertainties assumed by the track fitter during reconstruction. The pull width, defined as the  $\sigma$  of the Gaussian fit, is larger than the expected for the local  $x$  direction by 18% in the barrel and 6% in the end-cap. The error scaling procedure corrects the pull distributions (Figures 14(b) and 14(d)). The pull widths before and after error scaling, as well as the error scaling values, for all detectors and measurement directions are given in Table 3. The Pixel barrel (end-cap) local X correction of 4.5 (3.6)  $\mu\text{m}$  corresponds to 41 (19)% of the genuine distribution width,  $\sigma_0$ . Adding those values in quadrature to the intrinsic resolution, is equivalent to enlarging the Pixel cluster uncertainty by 7.9 (1.8)%. Error scaling corrections for the Pixel barrel local  $y$  residuals are comparable. In the end-cap, however, given that the initial pull width is already less than unity, no correction is applied. For the SCT, barrel (end-cap) corrections are 7 (6)%, while in the TRT barrel and end-cap the error scaling is fixed to zero as the initial pull width is less than one (see Figure 16).

Detector	Pull $\sigma$ before	Pull $\sigma$ after	C ( $\mu\text{m}$ )
Pixel Barrel X	1.18	1.00	4.5
Pixel Barrel Y	1.13	1.00	33.5
Pixel End-cap X	1.06	1.00	3.6
Pixel End-cap Y	1.00	0.99	0
SCT Barrel	1.08	1.00	8.1
SCT End-cap	1.07	1.00	8.7
TRT Barrel	0.96	0.96	0.0
TRT End-cap	0.96	0.96	0.0

Table 3: Pull widths before and after error scaling, and the associated C value.

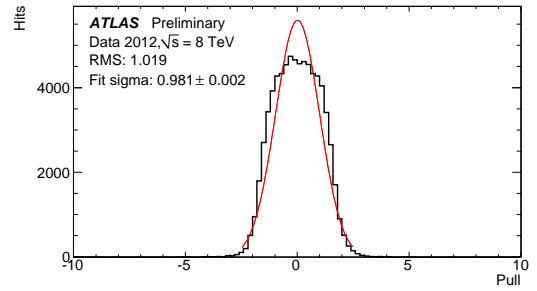
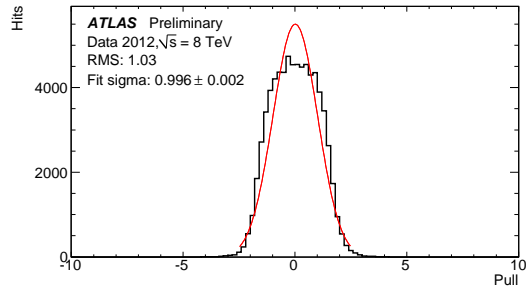
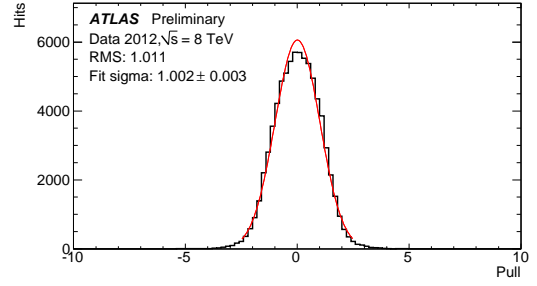
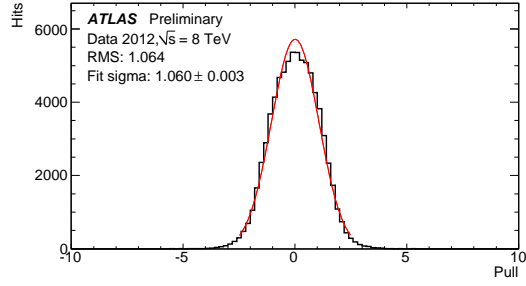
<sup>4</sup>A linear track fit treats all measurement uncertainties to be Gaussian.





(a) Pixel barrel: residual pulls before correction.

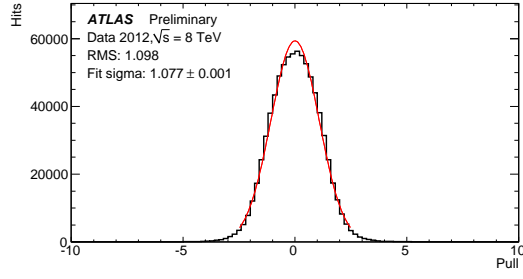
(b) Pixel barrel: residual pulls after correction



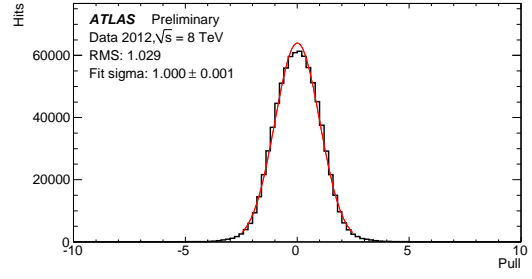
(c) Pixel end-caps: residual pulls before correction

(d) Pixel end-caps: residual pulls after correction

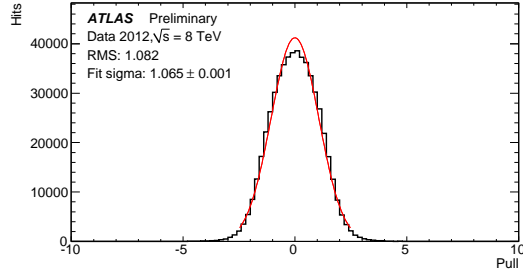
Figure 14: Pixel local  $x$  (upper plot in a pair) and local  $y$  (lower plot in a pair) residual pull distributions before and after error scaling correction.



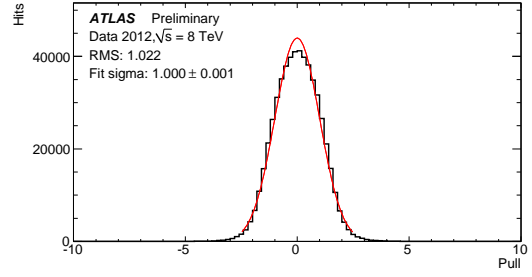
(a) SCT barrel: residual pull before correction.



(b) SCT barrel: residual pull after correction.

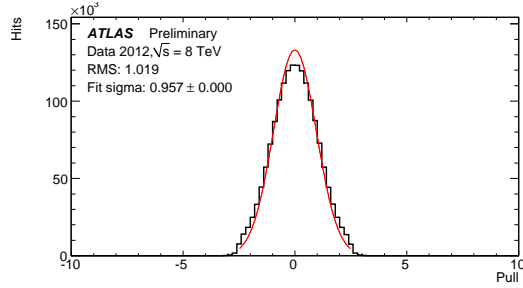


(c) SCT end-caps: residual pull before correction.

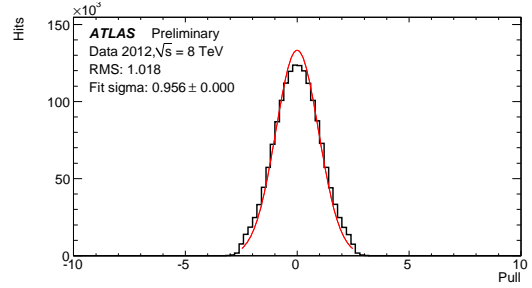


(d) SCT end-caps: residual pull after correction.

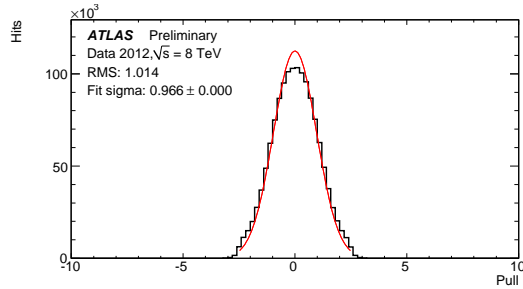
Figure 15: SCT local  $x$  residual pull distributions before and after error scaling correction.



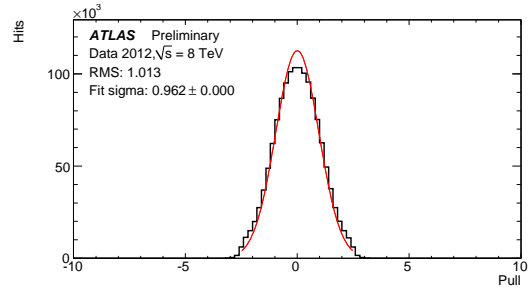
(a) TRT barrel: residual pull before correction.



(b) TRT barrel: residual pull after correction.



(c) TRT end-caps: residual pull before correction.



(d) TRT end-caps: residual pull after correction.

Figure 16: TRT residual pull distributions before and after error scaling correction.

## 6 Momentum Biases

Momentum biases can generally be classified into two categories: *sagitta* and *radial* biases. *Sagitta* deformations, which consist of detector movements orthogonal to the track trajectory, and hence affect the reconstructed track curvature oppositely for positively and negatively charged particles, can be divided into two further categories: deformations that do and do not affect the  $\chi^2$  of a track fit. The former should be removed by the alignment procedure, unless the alignment procedure is not performed at fine enough granularity or frequently enough. The latter cannot be completely removed with use of track-based alignment alone and require additional information for detection and elimination. *Radial* biases are characterized by detector movements along the track trajectory and are typically difficult to remove due to the small impact they have on the  $\chi^2$  of a track fit.

### 6.1 Sagitta Biases

Orthogonal displacements of the reconstructed hits in the detector result in a charge-antisymmetric alteration of the track curvature, which translates into a shift of the measured transverse momentum according to:

$$q/p_T \longrightarrow q/p_T + \delta_{\text{sagitta}} \quad \text{or} \quad p_T \longrightarrow p_T(1 + qp_T \delta_{\text{sagitta}})^{-1}. \quad (7)$$

The  $\delta_{\text{sagitta}}$  is a universal bias parameter for all measured momenta and uniquely defines the deformation. As the reconstructed polar angle does not change, the longitudinal component of the momentum scales in an identical manner to the transverse component, leading to:

$$p \longrightarrow p(1 + qp_T \delta_{\text{sagitta}})^{-1}. \quad (8)$$

Two methods are used for the determination of the sagitta biases. The first one uses the electromagnetic calorimeter as a reference and utilises the ratio of the measured energy deposited in the calorimeter ( $E$ ) and of the momentum as measured by the ID ( $p$ ) of electrons. Under the assumption that the calorimeter response is independent of the charge of the incoming particle, charge-dependent momentum biases introduced by the alignment procedure in the ID are expected to be seen as differences in the  $E/p$  ratio for electrons and positrons [6]. The second method is an iterative technique using  $Z \rightarrow \mu\mu$  candidates. This method extracts the magnitude of the individual track momentum biases by characterizing the shifts in the reconstructed  $Z$  invariant mass throughout the different detector regions. This method is particularly good at identifying local sagitta biases but is relatively insensitive to the global biases as they are only a second order correction to the reconstructed invariant mass [6]. The results shown in this section have been obtained using  $8.3 \times 10^6$   $Z \rightarrow \mu\mu$  events and  $5.4 \times 10^6$   $Z \rightarrow ee$  events.

The measured sagitta biases are minimized during the determination of the baseline alignment constants by adding constraints to the parameters of the tracks used to perform the alignment [6, 20]. These constraints are based on the results obtained from the  $Z \rightarrow \mu\mu$  with an additional correction applied to the global sagitta bias which is obtained from the  $E/p$  method.

Figure 17(a) shows sagitta biases in  $40 \times 40$  bins in  $\phi$  vs  $\eta$  as obtained using the  $E/p$  ratio method. In both end-caps there are small localized momentum biases. In the negative end-cap (side C) there is a deformation which amounts to approximately  $-0.6 \text{ TeV}^{-1}$  or 3% at  $p_T = 50 \text{ GeV}$ . Similar features are observed in the positive end-cap (side A) around  $\eta = 2.5$ . Figure 17(b) shows the distribution of observed sagitta biases. The mean sagitta bias is  $0.023 \text{ TeV}^{-1}$  with an RMS of  $0.14 \text{ TeV}^{-1}$ , which translates into a mean bias of 0.12% and an RMS of 0.7% at  $p_T = 50 \text{ GeV}$ <sup>5</sup>.

Figure 18 shows the sagitta biases measured using the  $Z \rightarrow \mu\mu$  method. Qualitatively the results look similar to those of the  $E/p$  method. Overall the mean sagitta bias is  $-0.009 \text{ TeV}^{-1}$  with an RMS

---

<sup>5</sup>It should be noted that non-negligible statistical fluctuations may contribute to the RMS

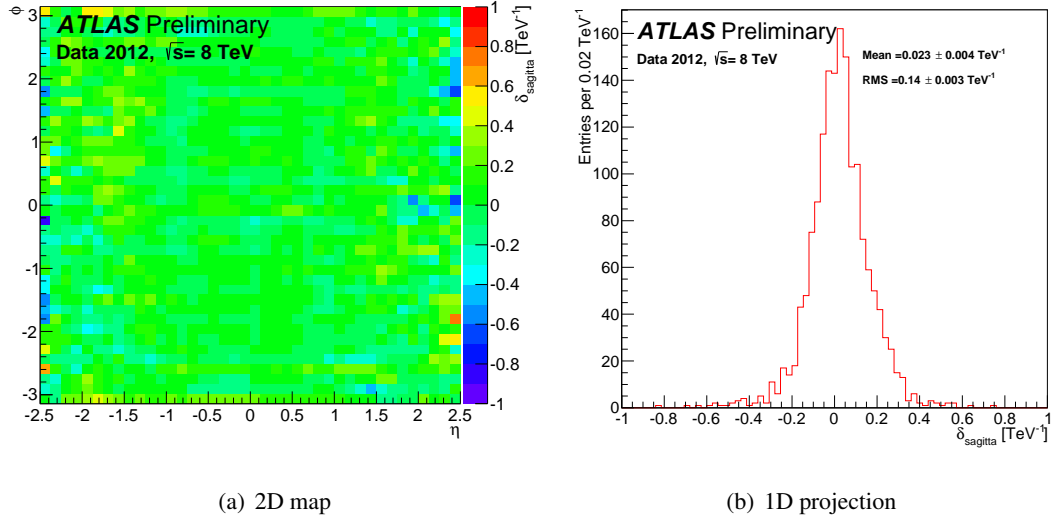


Figure 17: The measured momentum bias ( $\delta_{\text{sagitta}}$ ) using the  $E/p$  method in 2012 data. The measurement is performed in  $40 \times 40$  regions of  $\eta$  and  $\phi$ . Figure 17(b) shows the results of the 1600 measurements performed.

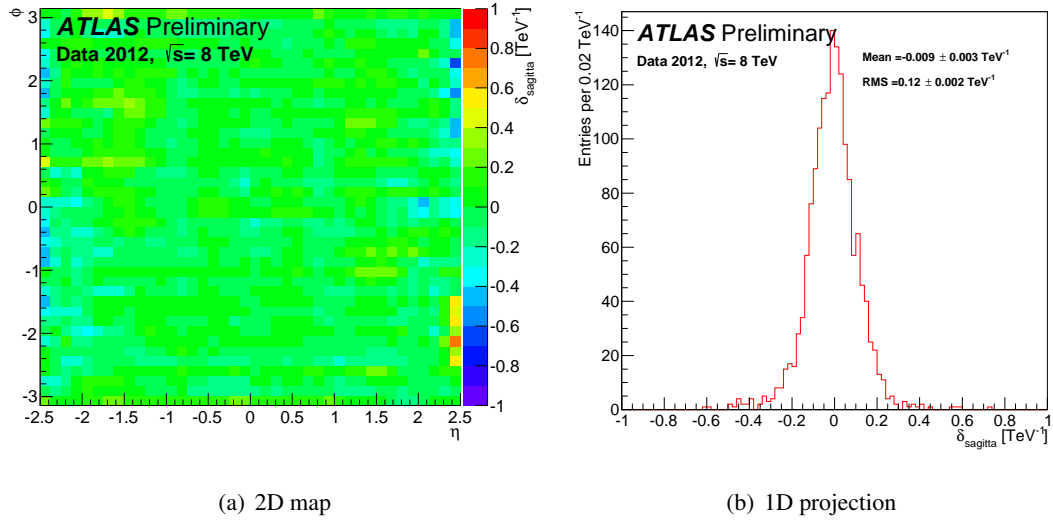


Figure 18: The measured momentum bias ( $\delta_{\text{sagitta}}$ ) using the  $Z \rightarrow \mu\mu$  method in 2012 data. The measurement is performed in  $40 \times 40$  regions of  $\eta$  and  $\phi$ . Figure 18(b) shows the results of the 1600 measurements performed.

of  $0.12 \text{ TeV}^{-1}$ , which translates into a mean bias of 0.05% and an RMS of 0.6% at  $p_T = 50 \text{ GeV}$ . The mean bias observed is significantly different from that of the  $E/p$  method, this can be attributed to the reduced sensitivity of the  $Z \rightarrow \mu\mu$  method to global sagitta biases (second order effect on the reconstructed invariant mass).

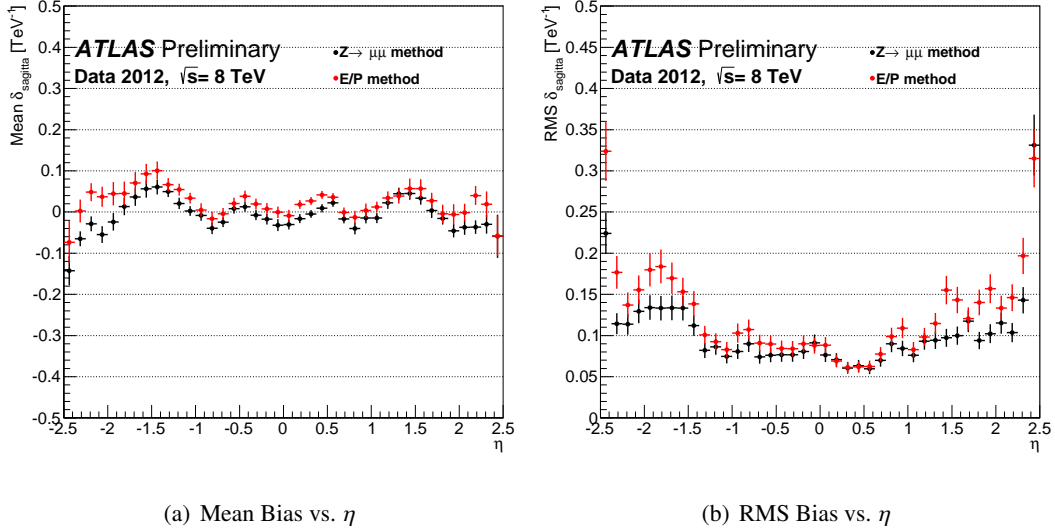


Figure 19: A comparison of the measured momentum bias ( $\delta_{\text{sagitta}}$ ) using the  $Z \rightarrow \mu\mu$  and  $E/p$  method in 2012 data.

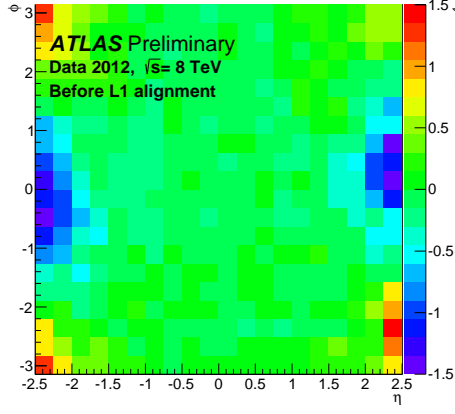
A comparison of both methods used to determine the sagitta bias as a function of  $\eta$  is shown in Figure 19. The mean sagitta shows clear indications of an  $\eta$  dependent structure. Once the global offset of  $Z \rightarrow \mu\mu$  results is taken into account, both methods produce compatible results. The overall sagitta bias of  $-0.009 \text{ TeV}^{-1}$ , corresponds roughly to a  $3 \mu\text{m}$  distortion at 1 m which is within the uncertainties of the alignment (see [6] for details).

## 6.2 Impact of Run-by-Run alignment on Sagitta Biases

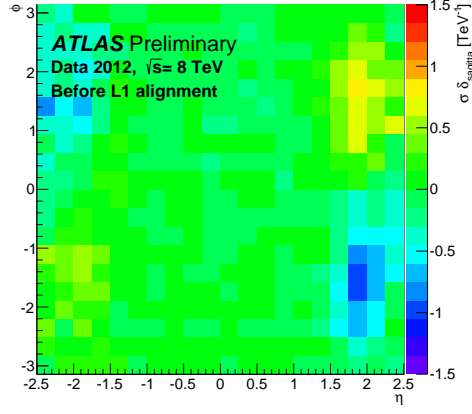
As noted earlier, the experience gained with the observed detector movements in 2011 resulted in a change in alignment strategy for the 2012 data-taking. In 2012, significant detector movements were automatically corrected for in the alignment and used for the initial data processing. As a result of this improved procedure the observed time-dependent sagitta biases for 2012 are significantly reduced. The main improvement originates from the correction of the movements of the end-caps with respect to the barrel detector. Figure 20 shows the impact of the alignment correction for two representative periods of ATLAS data-taking, referred to as periods A (April 4<sup>th</sup>–16<sup>th</sup> 2012) and H (October 13<sup>th</sup>–26<sup>th</sup> 2012).

Despite the minimal change in the average sagitta bias both inclusively and as a function of  $\eta$  (see Figure 21) before or after corrections, a measurable improvement in the momentum resolution is observed due to the reduction of the  $\phi$ -dependent structure. In both periods A and H the spread of the sagitta biases has reduced by over 50% as a result of the alignment corrections.

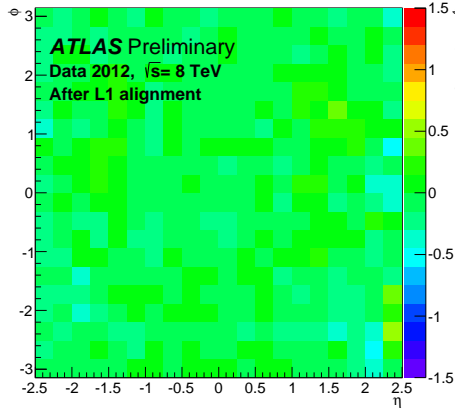
These results validate the adopted strategy, where by detailed alignment at all levels of granularity with explicit removal of sagitta distortions is performed only in the chosen reference data-taking period (see Sec. 3.4). This alignment is then propagated to other periods via *Level 1* corrections only, which account for the bulk of physical detector movements due to environmental changes. It has also been verified that higher level alignment corrections can give only marginal improvement on top of the adopted



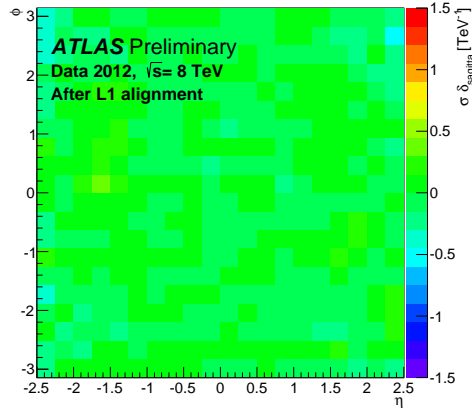
(a) Period A before end-cap alignment



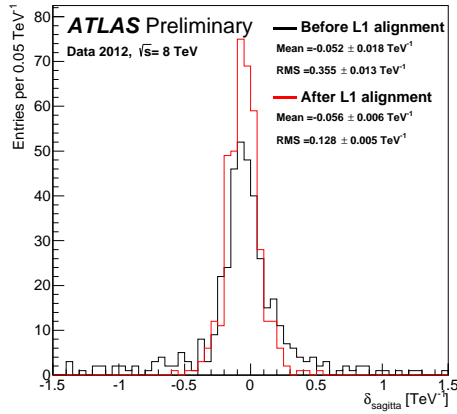
(b) Period H before end-cap alignment



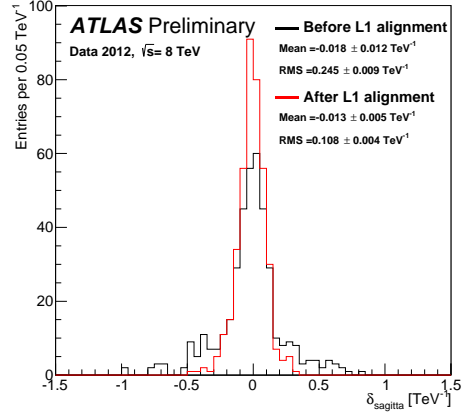
(c) Period A after end-cap alignment



(d) Period H after end-cap alignment



(e) Projection of the measured bias in period A



(f) Projection of the measured bias in period H

Figure 20: The measured momentum bias ( $\delta_{\text{sagitta}}$ ) using the  $Z \rightarrow \mu\mu$  method in 2012 data for various periods of time. The measurement was performed in  $20 \times 20$  regions of  $\eta$  and  $\phi$ . It should be noted that a non-negligible statistical fluctuations may be present in these measurements (up to  $0.1 \text{ TeV}^{-1}$  for the high  $\eta$  regions)

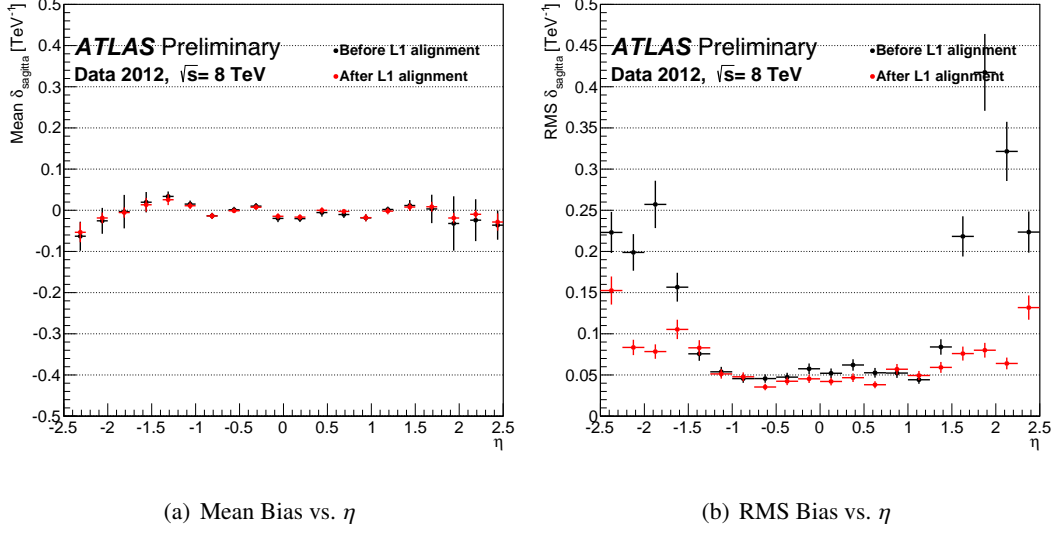


Figure 21: A comparison of the measured momentum bias ( $\delta_{\text{sagitta}}$ ) using the  $Z \rightarrow \mu\mu$  Period H before and after L1 alignment corrections.

procedure.

### 6.3 Charge-symmetric deformations

An example of charge-symmetric deformations are *radial* distortions. These affect the measured momentum via the radial expansion/contraction of the measured trajectory. In general they can be described as the direction-dependent radial scaling  $r \rightarrow (1 + \epsilon_{\text{radial}}(\phi, \eta))r$ . The lowest-order mode is a radial expansion/contraction and does not usually occur due to other constraints on the geometry.

As it was in the case of the *sagitta* distortion, the generic radial expansion is not an exact weak mode but it approximates one for large momenta. Radial scaling affects particles of both charges symmetrically. The geometrical transformation in the radial plane leads to an approximate change of the measured transverse momentum according to:

$$p_T \rightarrow p_T(1 + \epsilon_{\text{radial}})^2 \cong p_T \rightarrow p_T(1 + 2\epsilon_{\text{radial}}) \quad \text{for small } \epsilon_{\text{radial}}. \quad (9)$$

The polar angle is not maintained and both result in the following scaling of the longitudinal component of the reconstructed momentum:

$$\cot\theta \rightarrow \cot\theta(1 + \epsilon_{\text{radial}})^{-1} \quad \text{hence} \quad p_z \rightarrow p_z(1 + \epsilon_{\text{radial}}). \quad (10)$$

What is reported in the following is the fractional momentum bias,  $\delta_{\text{radial}}$ , which is defined such that  $p \rightarrow p(1 + \delta_{\text{radial}})$ .

In contrast to the sagitta distortions described earlier, the momentum bias is proportional to the change in the radial scale, and independent of the momentum. For this reason, low-momentum tracks are just as sensitive to radial deformations as high-momentum ones. Radial distortions lead to visible shifts in the reconstructed mass of decaying particles. The study presented here is performed on the full 2012 dataset which contains 40 M  $J/\psi$  candidates. The momentum scale is determined by performing a maximum-likelihood fit of the data to simulated invariant mass templates obtained from MC simulation.

Background contamination is taken into account by simultaneously fitting a polynomial in the template fit. The signal template, which is taken from Monte Carlo simulation, is convoluted with a Gaussian.

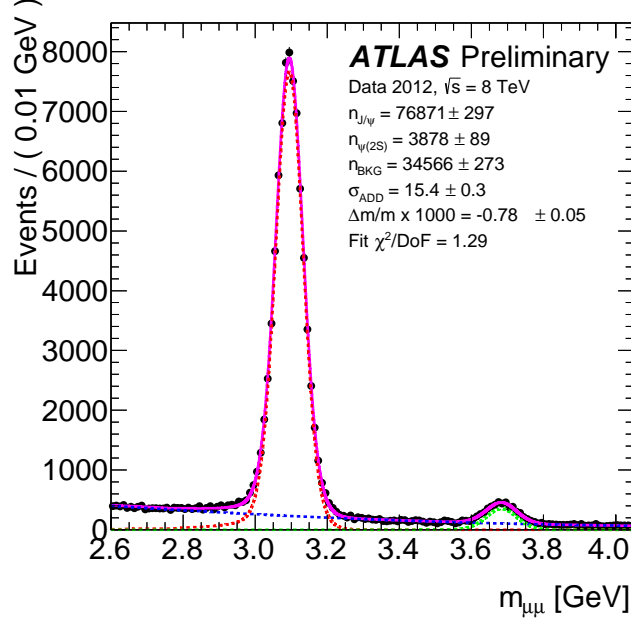


Figure 22: An example of the template fit in the region  $0 \leq \eta \leq 0.25$ .

The mean of this Gaussian is equal to the fractional bias in the measured mass ( $\delta m/m$ ) and correlated to biases in the measured momentum. The width of the Gaussian ( $\sigma_{\text{ADD}}$ ) is equal to the additional smearing required for the MC simulation to match the data<sup>6</sup>. Additional fit parameters include the number of background, signal and  $\psi(2S)$  events that fall within the fit window of 2.6 GeV to 4.05 GeV. An example of the fit can be seen in Figure 22.

To determine if the momentum biases vary as a function of the direction of a track the  $J/\psi$  mass is measured as a function of each muon's direction. Initially, the measured invariant mass bias is attributed to originate from an equal bias on the two muons momenta. As there are two muons contributing to the reconstructed mass and it cannot be assumed that both muons are biased in the same manner (unless they pass through the same region of the detector) and as such the reconstructed mass may not be a true reflection of any one muon's momentum bias. In order to account for the correlation between the bias in the reconstructed mass and biases in the momenta of the two muons, the measurement is iterated by adding momentum corrections determined in the current iteration to the results of the previous iteration and repeating the measurement.

Figure 23 shows the measured momentum scale offset  $\delta_{\text{radial}}$ , measured using the  $J/\psi$ , as a function of  $\eta$ , while in Figure 24 the  $\eta$  and  $\phi$  dependence is shown. Differences in the momentum scale are also seen between silicon only tracks when compared to full length ID tracks, indicating that both the silicon and the TRT parts are radially misaligned in a way which is not entirely consistent with each other.

The ID momentum scale bias amounts to approximately  $-0.085\% \pm 0.005\%$ . This difference, if assumed to be originating from a purely radial deformation like that described in equations 9 and 10 would translate into a radial bias of about  $-1.6$  mm over the full radius of the Inner Detector. Another potential source of momentum scale biases could be the magnetic field strength. This has been measured to be accurate to 0.02% to 0.12% depending on the track rapidity [29]. Currently, no explicit corrections are applied to the alignment to remove these biases.

<sup>6</sup> $\sigma_{\text{ADD}}$  could potentially be used to measure the momentum smearing.



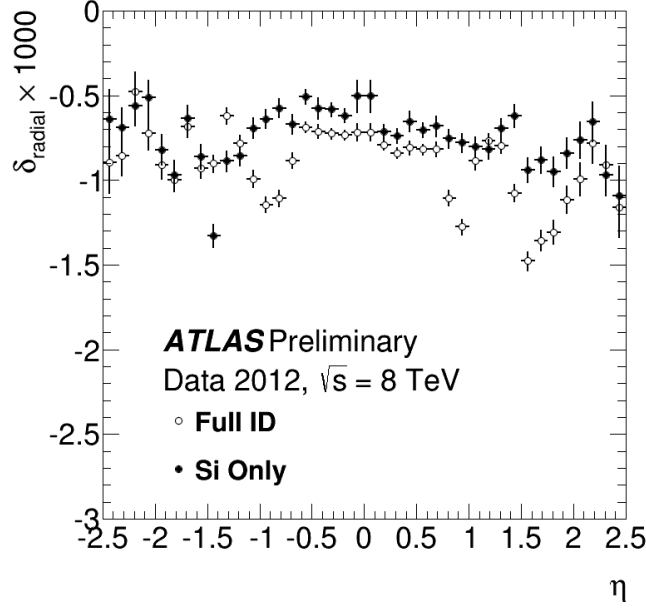


Figure 23: The momentum scale derived using  $J/\psi \rightarrow \mu\mu$  events as a function of  $\eta$  for both tracks with only silicon hits (solid circles) and for complete ID tracks (open circles).

## 7 Momentum Resolution

### 7.1 Method

The ID momentum resolution is measured using a pure sample of muons produced in  $Z$  decays. The  $Z \rightarrow \mu^+\mu^-$  decays are selected using the event and track selection described in Section 4.1. In addition, tracks are required to be isolated by requiring that the sum of the  $p_T$  of all tracks in a cone of size  $\Delta R < 0.3$  be less than 0.05 of the muon  $p_T$ . Finally, to select tracks identified as muons by the Muon Spectrometer [2], it is required that each muon candidate has at least 3 hits per station in at least 2 stations (out of 3) of the barrel or end-cap Muon Drift Tubes (MDTs), or at least 3 hits in the end-cap, middle and outer MDTs, along with at least 2 Cathode Strip Chamber  $\eta$  hits. Finally, at least one  $\phi$  hit in two different subsystem layers is required.

The fractional momentum resolution is given as a function of the muon's transverse momentum  $p_T$  and pseudorapidity  $\eta$ . Its parameterisation is designed to model various effects that contribute to the momentum resolution, namely the multiple scattering in the traversed material and the intrinsic spatial resolution. The function used to describe the fractional momentum resolution is given by the product of two terms:

$$\sigma(1/p)/(1/p) = F(p_T) \times f(\eta, p_T). \quad (11)$$

The first term, which describes the  $p_T$  dependence of the resolution, can be written as the sum in quadrature of two components:

$$F(p_T) = p_1^{\text{ID}} \oplus (p_2^{\text{ID}} \times p_T), \quad (12)$$

where  $p_1^{\text{ID}}$  is the multiple scattering term in the ID, and  $p_2^{\text{ID}}$  describes the intrinsic resolution. The parameters  $p_1^{\text{ID}}$  and  $p_2^{\text{ID}}$  are fitted separately in data and Monte Carlo simulation using an unbinned maximum likelihood fit to the  $Z \rightarrow \mu^+\mu^-$  invariant mass.

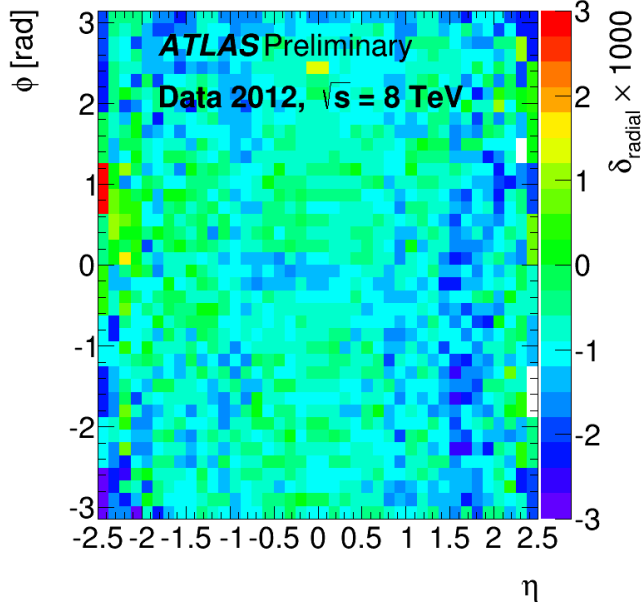


Figure 24: The measured radial momentum biases using  $J/\psi$  events bins of  $\eta$  and  $\phi$ .

The dependence in  $\eta$  of the resolution is described by the function  $f(p_T, \eta)$ , which is parameterised as a polynomial function with coefficients that are determined from a fit to the single muon resolution in the MC simulation. A separate fit for data is not considered necessary since the shape of  $f(p_T, \eta)$  is dominated by the description of the material in the detector, which is believed to be sufficiently accurately represented in the MC simulation. The function  $f(p_T, \eta)$  also has a small dependence on  $p_T$  which is used to improve the  $\eta$  parameterisation for high momentum muons.

The ID momentum resolution is measured by fitting the invariant mass distribution of the Z boson reconstructed with ID tracks only. By making use of an unbinned maximum likelihood fit to the Z boson mass that correctly parameterises each muon as a function of its  $p_T$  and  $\eta$  one can maximize the statistical power of the available data.

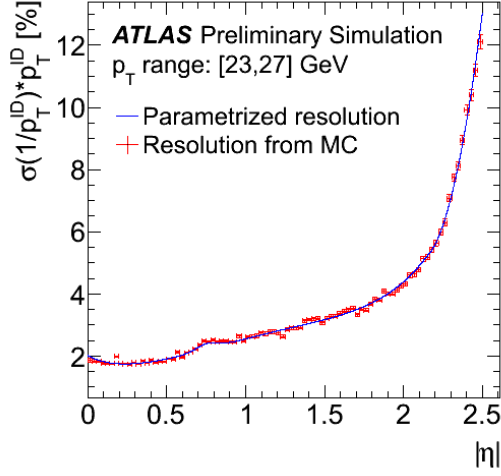
The fit to the Z boson invariant mass distribution is performed in the region  $70 < m_{\mu\mu} < 110$  GeV. The function used to describe the di-muon invariant mass in the fit is the convolution of a Gaussian, which describes the experimental resolution, with a function that accurately describes the Z line-shape, including the Z boson natural width, the photon radiation term, and the  $\gamma$ -Z interference term. Corrections for final state radiation (FSR) are implemented prior to the fit. These corrections, extracted from the MC simulation, are applied to both data and simulation.

The Z bosons intrinsic width and mass are fixed to the world averages [30], thus making the fit sensitive to a global  $p_T$  scale factor  $\alpha$ , with  $1/p_T \rightarrow 1/p_T(1 + \alpha)$ .

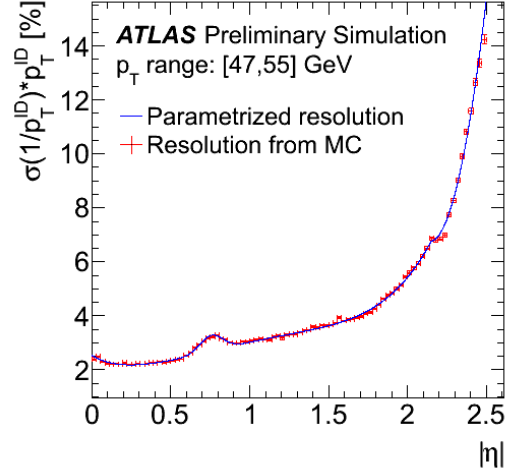
## 7.2 Results

The fractional momentum resolution  $\sigma(1/p)/(1/p)$  measured in the MC simulation is shown in Figure 25 for various  $p_T$  intervals. The result of the 2D parameterisation described in Equation 11 is also shown. The excellent agreement between the two distributions validates the method. This parameterisation provides an excellent description in all regions of the ID for transverse momenta between 15 and 400 GeV.

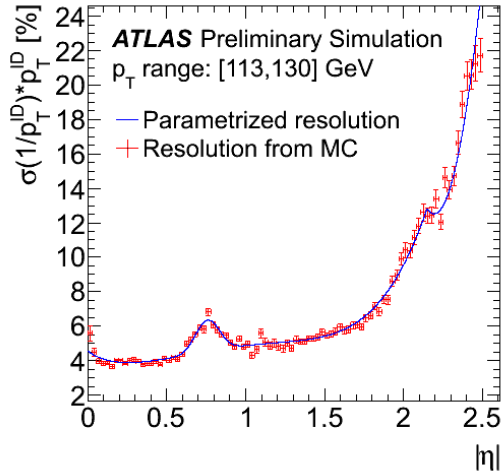
Figure 26 shows the fractional momentum resolution as a function of  $p_T$  fitted in data and MC simu-



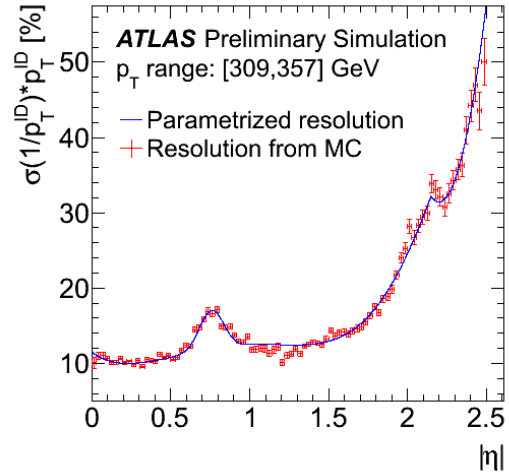
(a)  $23 \text{ GeV} \leq p_T \leq 27 \text{ GeV}$



(b)  $47 \text{ GeV} \leq p_T \leq 55 \text{ GeV}$

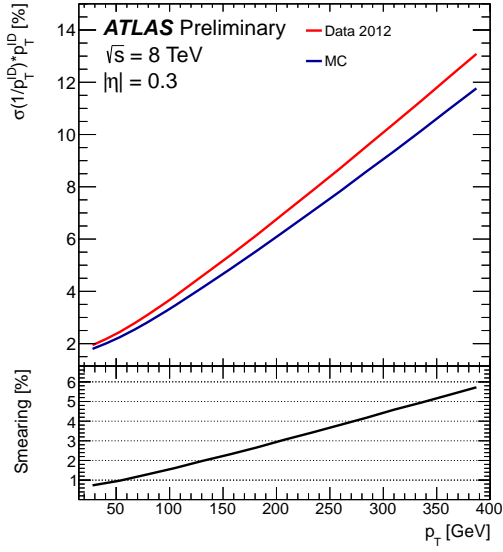


(c)  $113 \text{ GeV} \leq p_T \leq 130 \text{ GeV}$

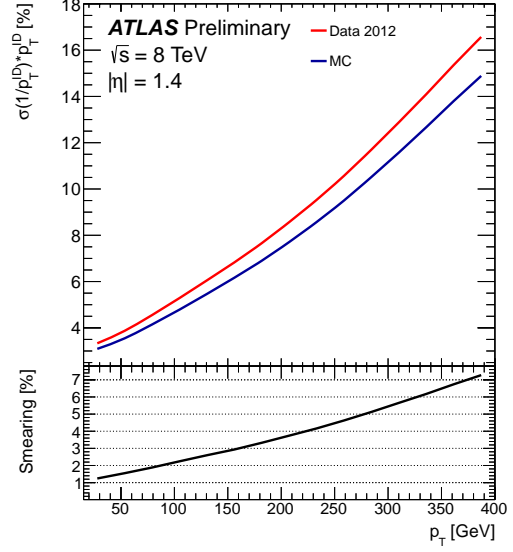


(d)  $309 \text{ GeV} \leq p_T \leq 357 \text{ GeV}$

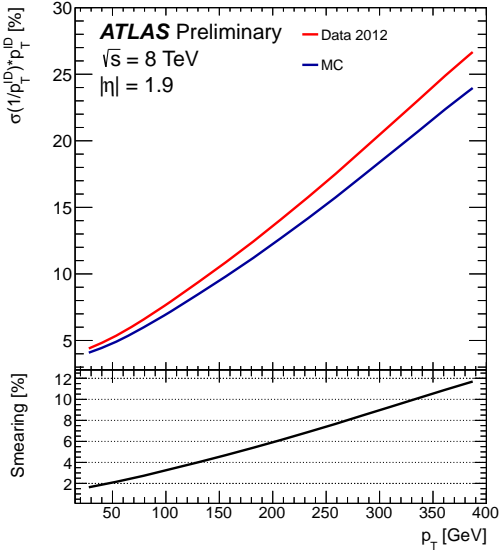
Figure 25: Fractional momentum resolution  $\sigma(1/p_T)/(1/p_T)$  as a function of pseudorapidity measured in the MC simulation in four  $p_T$  regions. The red dots with error bars show the fractional resolution in MC simulation and the blue line shows the projection of the fit obtained using the 2D parameterisation described in the text.



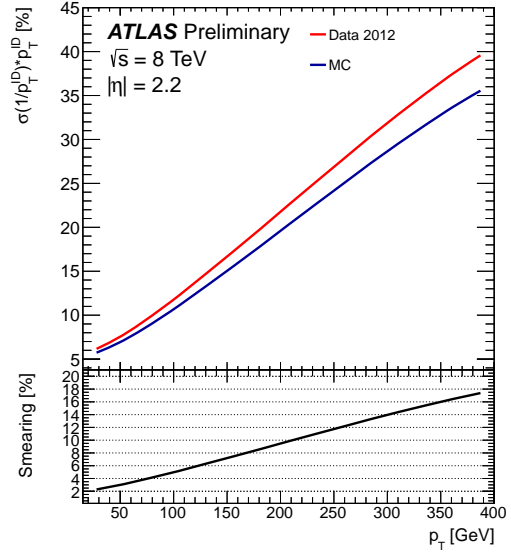
(a)  $\eta = 0.3$



(b)  $\eta = 1.4$



(c)  $\eta = 1.9$



(d)  $\eta = 2.2$

Figure 26: Fractional  $p_T$  resolution for data (red line) and MC simulation (blue line) as a function of  $p_T$  for four different values of pseudorapidity. The black line shows the smearing function that has to be added in quadrature to the MC simulation resolution in order to provide a good description of the resolution in data.

lation together with the resulting smearing function needed for the MC simulation in order to reproduce data. The intrinsic resolution term is measured to be 12% larger in data than in MC simulation. The dominant factor contributing to this difference in the momentum resolution is the difference in the Pixel hit resolution which is also observed in the Pixel residual distribution (see Section 4.5).

Figure 27 shows the distribution of the di-lepton invariant mass for data and for MC simulation after applying the smearing function described above. The bottom plot shows the agreement between data and

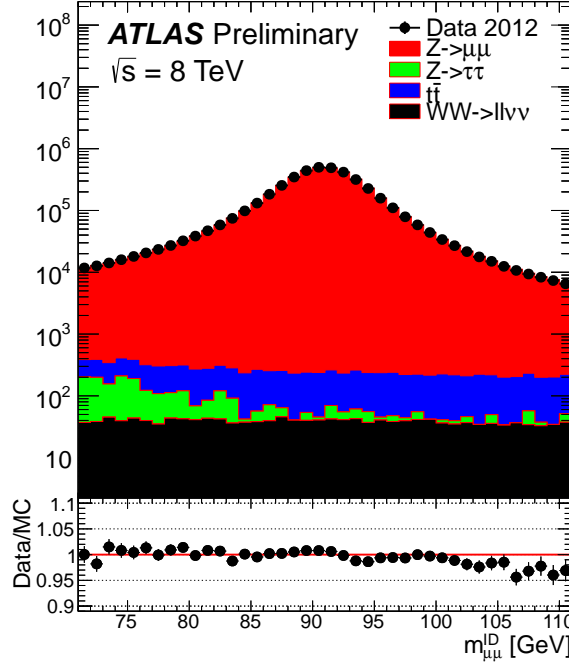


Figure 27: Data-MC comparison of the di-lepton invariant mass distribution after applying to the MC simulation the smearing function described in the text. The black points are data; the histogram is Monte Carlo simulation that includes  $Z \rightarrow \mu\mu$  (red),  $Z \rightarrow \tau\tau$  (green),  $t\bar{t}$  (blue), and di-boson (black) production.

MC simulation to better than 2% in most bins.

Figure 28 validates the parameterisation in  $\eta$  of the fractional momentum resolution. The figure shows the width of the Z invariant mass distribution as a function of the pseudorapidity of the leading muon for data and MC simulation before (left) and after (right) applying the smearing function to the MC simulation. The ratio between the two distributions is shown on the bottom plot, and indicates that the agreement between data and smeared MC simulation is better than 1% up to  $|\eta| = 2.3$ . For higher values of  $\eta$ , the width of the MC simulation exceeds that of the data, indicating that the momentum resolution has been overestimated in the simulation. Therefore, no smearing needs to be applied in the  $|\eta| > 2.3$  region.

Figure 29 validates the fit of the global  $p_T$  scale factor to be applied to the MC simulation to reproduce data,  $\alpha = 1.1 \pm 0.2\%$ . This value is compatible with other measurements of the  $p_T$  scale presented in this note (see Sec. 6.3). The fractional difference between data and corrected MC simulation shown in the bottom plot is at the sub-permille level.

A detailed parameterisation of the resolution in data and MC simulation allows for a calibration of the uncertainties on  $1/p$  provided by the track fitter. The algorithm calculating these uncertainties uses as input detailed kinematical properties of each muon, and takes into account the amount of material traversed by the track, the number of hits, and the  $\chi^2$  of the fit.

The scaling factors are calculated as the relative difference between the parameterisation of the fractional resolution obtained with the method described above and the fractional resolution provided by the track fit. The obtained scaling factors are shown in Figure 30 as a function of  $\eta$  and  $p_T$  for muons with transverse momentum between 30 and 200 GeV. Data is shown on the left, while MC simulation is shown on the right. In both data and MC simulation, corrections are mostly needed in the pseudorapidity region  $|\eta|=0.5-0.7$ . Corrections in the forward regions  $|\eta| > 2$  are typically more contained.

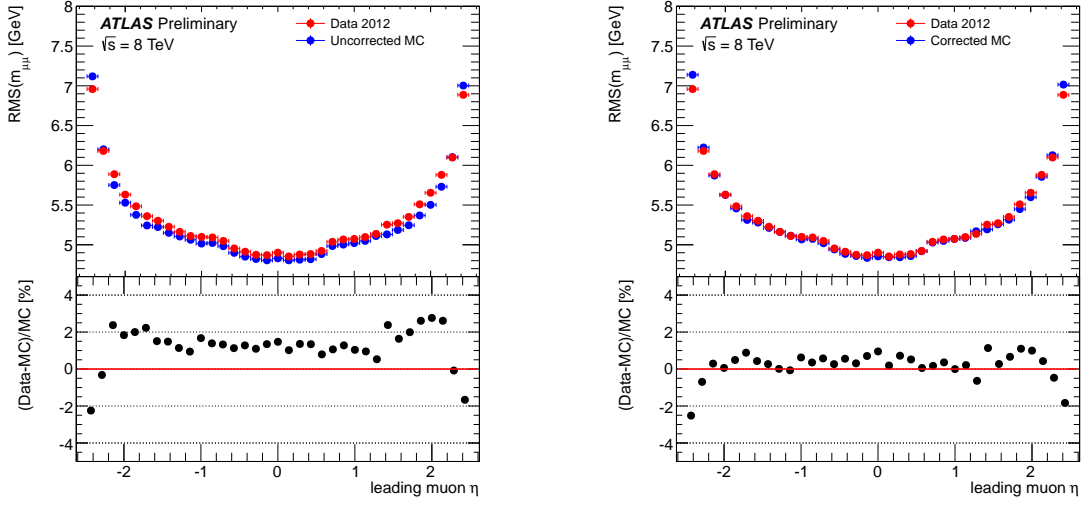


Figure 28: Data-MC comparison of the RMS of the dilepton invariant mass distribution as a function of  $\eta$  before (left) and after (right) correcting the MC simulation according to the procedure presented in this paper. The red points are data while the blue points are MC simulation. The bottom plots show that after smearing data and MC simulation are in agreement to better than 1%.

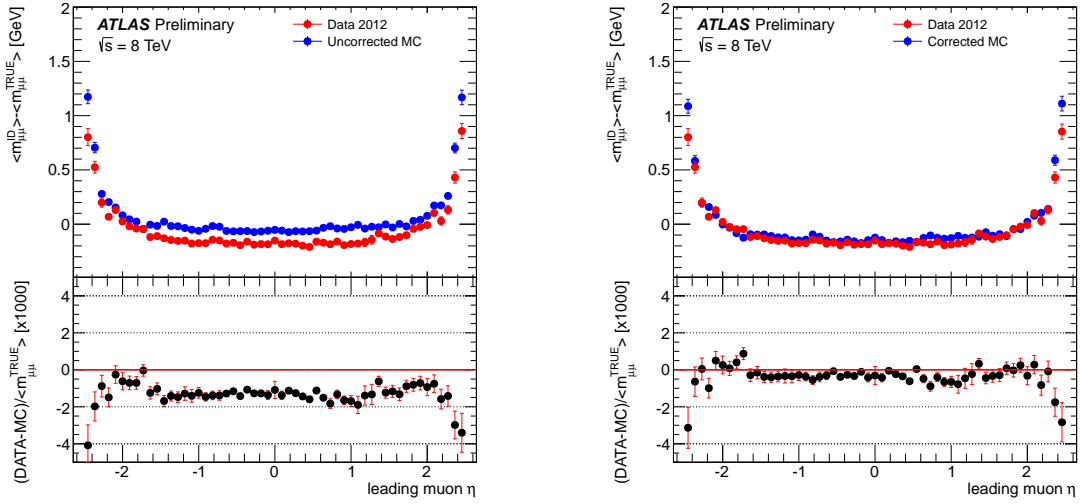


Figure 29: Data-MC comparison of the mean of the dilepton invariant mass  $m_{\mu\mu}$  distribution as a function of  $\eta$ . Red dots represent data. Blue dots represent MC simulation before (left) and after (right) applying the smearing procedure described in the paper. The bottom plots show that the data-MC agreement is better than 1%.

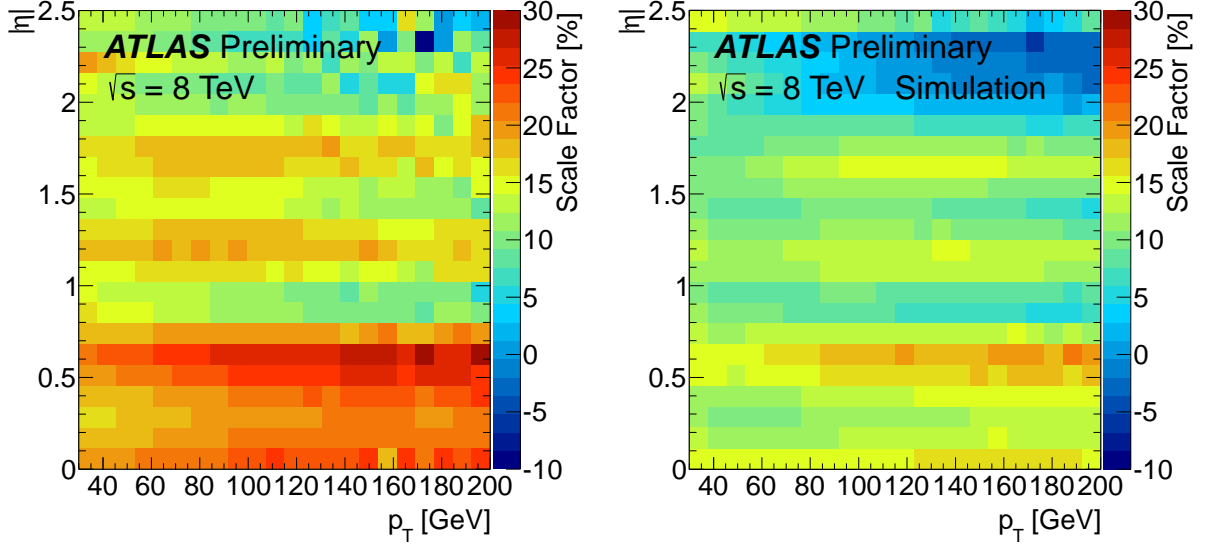


Figure 30: Calibration factors to be applied to the momentum uncertainties provided by the track fitter. They are calculated bin-by-bin as the percentage difference between the parameterisation of the fractional resolution obtained with the method described in this document and the fractional resolution provided by the track fitter. Data is shown on the left, while MC simulation is shown on the right.

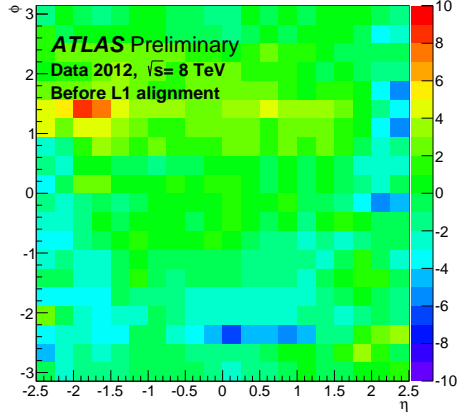
## 8 Impact Parameter Biases

The transverse and longitudinal impact parameter (IP) of a track,  $d_0$  and  $z_0$ , are the distance of closest approach to the primary vertex in the transverse and longitudinal plane, respectively. They are key ingredients for distinguishing tracks originating from displaced vertices from tracks originating from the primary collision.

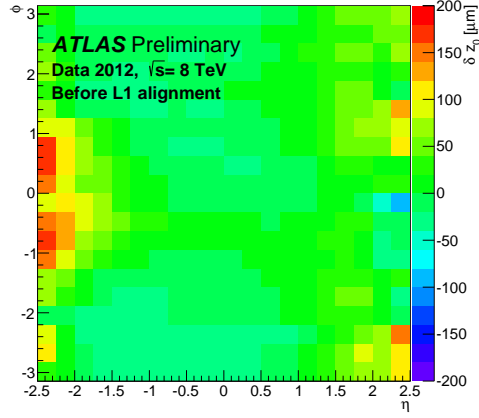
Detector distortions and remaining misalignments may lead to biases on the reconstructed impact parameters. These biases affect a number of physics measurements such as lifetime measurements and vertex reconstruction. A simple and robust way of measuring any potential bias is to use the tracks from  $Z \rightarrow \mu^+\mu^-$  boson decays. An iterative procedure was used to determine the IP biases. In an analogous way to the one used for the determination of the sagitta biases using  $Z$  boson decays, the IP biases can be measured by applying corrections to the measured impact parameters until the difference between the impact parameters of the two muons originating from a  $Z$  boson is, on average, zero.

The results are obtained using the entire 2012  $Z \rightarrow \mu^+\mu^-$  dataset and the selection criteria for the  $Z$  boson candidates described in Section 4.1. The biases prior to corrections for both  $d_0$  and  $z_0$  parameters are shown in Figures 31(a) and 31(b) as a function of  $\eta$  and  $\phi$ . The bias observed in  $z_0$  is most pronounced in the end-caps reaching about  $150 \mu\text{m}$  in the negative  $\eta$  end-cap, while the initial bias in  $d_0$  has a maximum of  $8 \mu\text{m}$ .

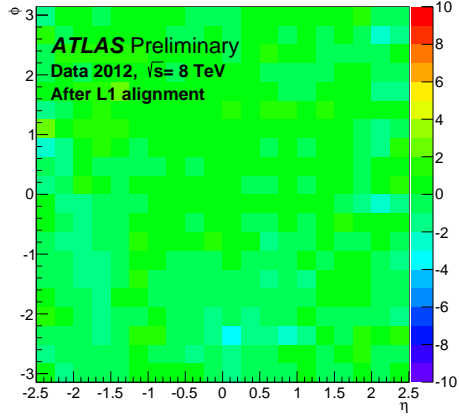
The observed impact parameter biases are corrected by adding constraints on the parameters of the tracks used to perform the alignment. The alignment constants obtained with this constraint are used to measure again the remaining impact parameter biases. The results are shown in Figures 31(c) and 31(d). The mean bias is reduced by about 80% in  $d_0$  and by 85% in  $z_0$ , and the RMS of the bias distribution, is reduced approximately by 60% in  $d_0$  and by 80% in  $z_0$ . This large improvement in the impact parameter biases is shown in Figures 31(e) and 31(f).



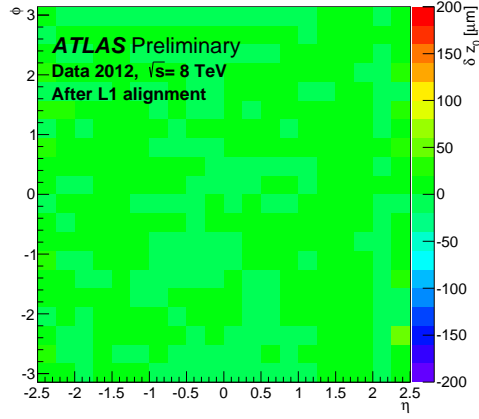
(a)  $\delta d_0$  bias before alignment



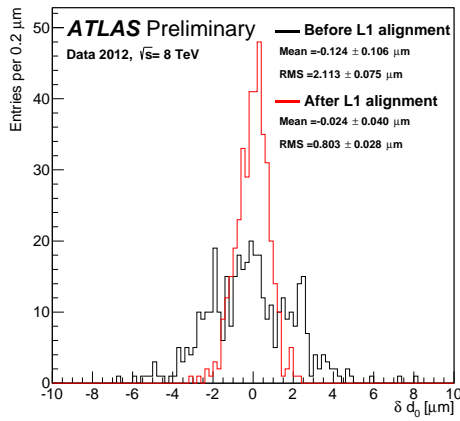
(b)  $\delta z_0$  bias before alignment



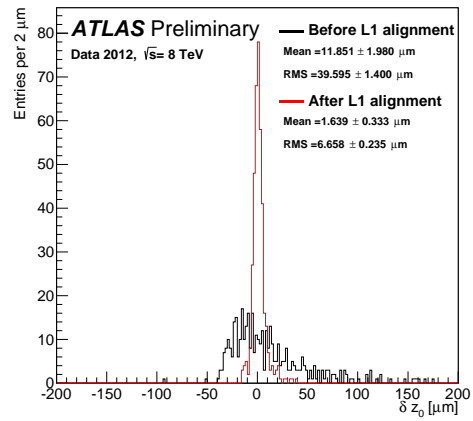
(c)  $\delta d_0$  bias after alignment



(d)  $\delta z_0$  bias after alignment



(e) Transversal impact parameter



(f) Longitudinal impact parameter

Figure 31: Average transverse and longitudinal impact parameter bias in  $20 \times 20$  bins in  $\eta$  and  $\phi$ . Before the impact parameter constrained alignment (a) and (b) and after the alignment (c) and (d). Histograms of the above maps are reported in plots (e) and (f), with distributions before and after the impact parameter constrained alignment overlaid.



## 9 Impact Parameter Resolution

In general, it is not possible to measure the impact parameter resolution  $\sigma_{\text{IP}}^{\text{track}}$  directly due to its convolution with the resolution on the primary vertex position,  $\sigma_{\text{IP}}^2 = \sigma_{\text{track}}^2 + \sigma_{\text{PV}}^2$ , where  $\sigma_{\text{PV}}^2$  is the projection of the primary vertex uncertainty along the axis of closest approach of the track to the primary vertex on the transverse or longitudinal plane.

This study is based on a limited, but representative, fraction of proton-proton collisions at  $\sqrt{s} = 8$  TeV data collected in 2012 with nominal magnetic field conditions. These samples contain a sufficient number of tracks for this study and are selected from data periods in which the detector and the LHC conditions were stable. In particular the events considered are selected by all the triggers that require jets, missing transverse energy or  $\tau$  leptons. The simulated QCD samples used in this study are generated with PYTHIA8 [25] at  $\sqrt{s} = 8$  TeV. Simulated samples contain jets above a certain  $E_T$  cut-off. For the data-Monte Carlo comparisons simulated samples are required to have at least one jet with  $E_T > 500$  GeV.

Only tracks fulfilling the following basic track quality selection are used:

- the track must be included in the reconstructed primary vertex (PV) and at least 10 tracks must be used in the PV reconstruction,
- $p_T$  greater than 500 MeV,
- $|\eta| < 2.5$ ,
- at least two hits in the Pixel detector,
- at least seven hits in the Pixel and SCT detector.

Tracks are divided into different categories of transverse momentum, pseudorapidity and hit content to ensure a reasonably constant and Gaussian resolution within a single subset. Both the transverse and the modified longitudinal impact parameter ( $d_0$  and  $z_0 \sin \theta$ , respectively) resolutions are measured for each track category binned in:

- $\eta$ ,
- $1/(p_T \sqrt{\sin \theta})$ ,
- number of hits and shared hits in the first Pixel layer.

The pseudorapidity  $\eta$  has been chosen because the intrinsic detector resolution and hit pattern depend on it, and  $1/(p_T \sqrt{\sin \theta})$  has been chosen instead of bare  $p_T$  because it is directly linked to the contribution of multiple scattering to the impact parameter resolution which is modeled by:

$$\sigma_{d_0} = \sqrt{a^2 + \frac{b^2}{p^2 \sin^3 \theta}} \quad (13)$$

The third criterion selects tracks with zero, exactly one, and more than one b-layer (first layer of the Pixel detector) hits. The modified longitudinal impact parameter is used because it directly reflects the resolution in the direction orthogonal to the trajectory (direct analogue of the  $d_0$ ). Tracks from the very dense environment of high  $p_T$  hadronic jets are also considered in the study. There is a non-negligible probability that several hits merge into a single indistinguishable cluster (*shared hits*). The effect of a shared hit is an increased hit position uncertainty. If the shared hit is in the first layer of the Pixel detector, this leads to a deterioration of the impact parameter resolution. For this reason, each of these sub-categories is itself divided in sub-categories selecting tracks that have zero, one shared hit in the first

layer of the Pixel detector with another track, and one or more shared hits in the other silicon layers. The most prevalent category is the one with tracks that have one hit in the first layer of the Pixel detector and zero shared hits. In the following, results mainly for this category will be discussed.

In order to extract the correct impact parameter resolution from data, it is important to understand how to subtract PV reconstruction contribution to the IP resolution. The method used for this relies on an iterative deconvolution procedure [31]. For each iteration an approximation of the unfolded distribution is obtained by multiplying the measured impact parameter of each track by a correction factor. For instance, for the transverse impact parameter with respect to the PV:

$$d_{PV} \rightarrow d_{PV} \sqrt{\frac{(K\sigma_{d_0})^2}{(K\sigma_{d_0})^2 + \sigma_{PV}^2}} \quad (14)$$

where  $K$  is a correction factor that depends on the iteration index. For the first iteration  $K$  is equal to one. For each iteration,  $\sigma_{d_{PV}}$  can be evaluated fitting each  $d_{PV}$  distribution and for the  $i$ -th iteration it should be:

$$(\sigma_{d_{PV}})_i = K_i \sigma_{d_0} \sqrt{\frac{1 + \frac{(K_{i+1}\sigma_{d_0})^2}{\sigma_{PV}^2}}{1 + \frac{(K_i\sigma_{d_0})^2}{\sigma_{PV}^2}}} \quad (15)$$

and then calculate the new  $K$  for the next iteration.

In order to evaluate the width of the core of the  $d_{PV}$  distributions, and hence estimate the impact parameter resolution, a Gaussian fit to the entire distribution is first applied and the temporary mean ( $\text{mean}_{\text{tmp}}$ ) and sigma ( $\sigma_{\text{tmp}}$ ) are extracted. The second step consists of refitting the distribution within the new range defined as  $\text{mean}_{\text{tmp}} \pm 2 \cdot \sigma_{\text{tmp}}$ . The iterative procedure ends when the fitted  $\sigma_{d_{PV}}$  is stable within approximately 0.01%. About five iterations are needed for the  $K$  factor to converge to stable values. They approximately range from 0.8 to 1.2. The iterative procedure is verified on MC simulation. The impact parameter resolutions derived from reconstructed tracks in the MC simulation are consistent with those derived from Monte Carlo truth.

Figure 32 shows the data to MC simulation comparison for both the transverse and modified longitudinal impact parameter measured with respect to the primary vertex for tracks with one b-layer hit in the Pixel detector and no shared hits in the silicon detectors as a function of the pseudorapidity  $\eta$  for two different  $p_T \sqrt{\sin \theta}$  regions. The two regions are:  $p_T \sqrt{\sin \theta} > 20$  GeV and  $0.4 \text{ GeV} < p_T \sqrt{\sin \theta} < 0.5$  GeV.

A discrepancy is observed between data and simulation in the modified longitudinal impact parameter resolution in the low  $p_T \sqrt{\sin \theta}$  region (Figure 32c). The additional contribution with respect to what is predicted from the MC simulation is about  $20 \mu\text{m}$  both in the barrel region and in the end-caps. This discrepancy is related to the differences seen in the local  $y$  residuals of the Pixel barrel modules in data and MC simulation. The root cause of this has not been understood yet, but the problem is under investigation.

The observed discrepancies between data and simulation for high  $p_T$  tracks (Figure 32b), on the other hand, point to either or both the presence of residual misalignments in the detector and the mis-modeling of the intrinsic detector resolution in the simulation. The intrinsic resolution in the simulation is extremely sensitive to the detector modeling. This is especially relevant because the reconstruction of the cluster position is performed by a neural network algorithm [32], which is expected to provide an excellent resolution, but needs to be trained on MC simulated samples. This dependence on simulation may result in an over-optimistic estimate of the achievable resolution. Further studies are required to determine which of these two effects is the most relevant.

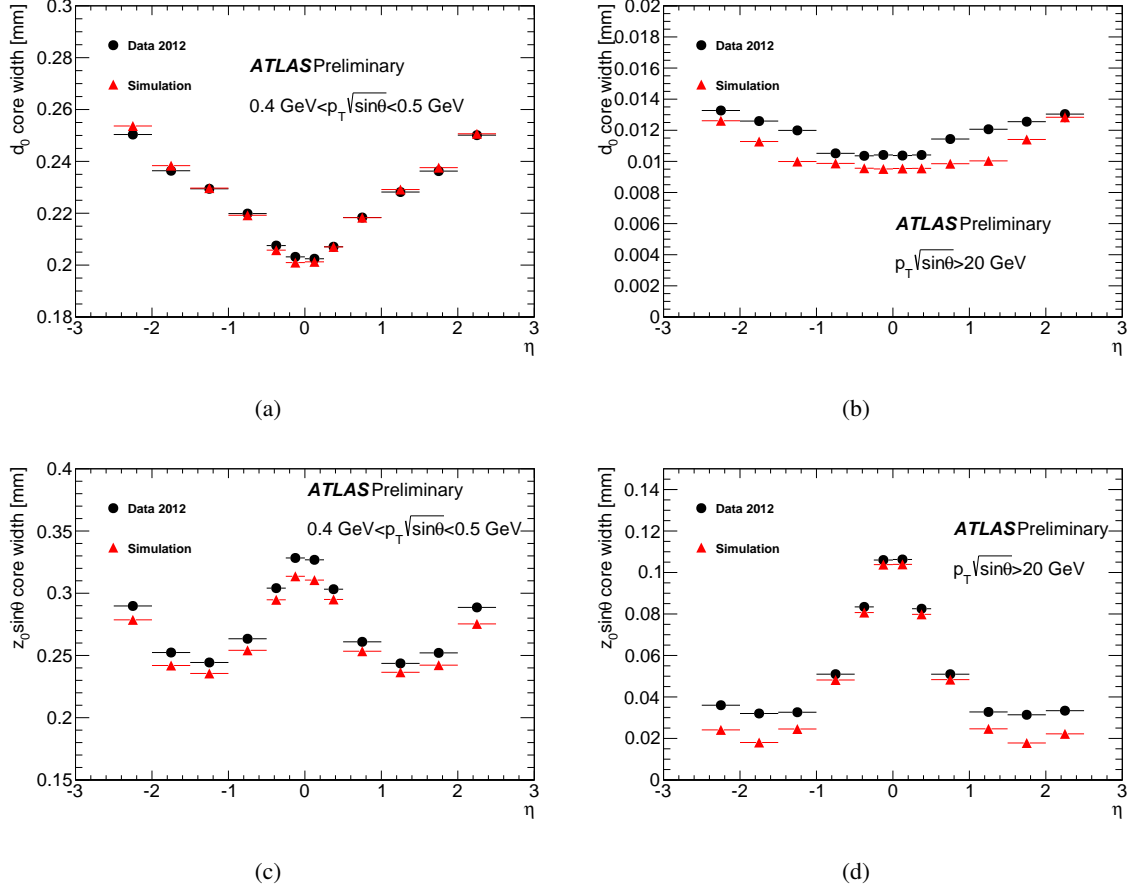


Figure 32: Core widths of the transverse (top) and modified longitudinal (bottom) impact parameters for tracks with one hit in the first layer in the Pixel detector and zero shared hits in the silicon detectors as a function of the pseudorapidity  $\eta$  for two different  $p_T \sqrt{\sin\theta}$  regions:  $0.4 \text{ GeV} < p_T \sqrt{\sin\theta} < 0.5 \text{ GeV}$  (a,c) and  $p_T \sqrt{\sin\theta} > 20 \text{ GeV}$  (b,d). The data (black dots) are compared to the MC simulation (red triangles). In all the plots only the statistical error is associated to each point, often smaller than the point itself.

## 10 Conclusion

The alignment strategy used for the track reconstruction of the LHC  $\sqrt{s} = 8 \text{ TeV}$  proton-proton collision data taken during 2012 has been presented. The baseline track-based alignment algorithm was enriched with the application of external constraints allowing for efficient suppression of systematic biases on the reconstructed momentum and measured impact parameters of charged particles. In addition, physical detector movements driven by occasional environmental changes were tracked at the level of large detector structures in order to minimize their impact on the reconstruction. The performance of the resulting alignment has been assessed using track-hit residual distributions, the reconstructed invariant mass of  $Z \rightarrow \mu^+ \mu^-$  and  $J/\psi \rightarrow \mu^+ \mu^-$  candidates, and the  $E/p$  ratio for electrons and positrons.

Medians of the modules track-hit residual distributions indicate that the individual sensing devices in all three ID subsystems (Pixel, SCT, and TRT) are aligned to better than  $1 \mu\text{m}$ . A comparison of the residual distribution between Data and MC simulation reveal discrepancies in the Pixel detector (seen mainly in the Pixel local  $y$  residuals). These are not likely to originate from misalignments and are under investigation. Measurements of the charge-antisymmetric momentum bias (sagitta deformation) show good uniformity across the entire acceptance of the detector. The average sagitta bias across the whole

detector corresponds to approximately a  $3\ \mu\text{m}$  distortion at  $1\ \text{m}$  radius, well within expected uncertainties of the alignment. The overall bias on the momentum scale (charge-symmetric momentum bias) of the Inner Detector tracking system has been measured to be  $-0.085\% \pm 0.005\%$ . No attempt to correct this bias within the alignment has been made. After the dedicated alignment, the bias on the reconstructed track impact parameter has been measured to be below a micron in the transverse direction and under  $10\ \mu\text{m}$  along the beam line.

Complementary studies of the charged particle momentum resolution and impact parameter resolution have been presented.

## References

- [1] L. Evans and P. Bryant, *LHC Machine*, JINST **3** (2009) S08001.
- [2] ATLAS Collaboration, *The ATLAS experiment at the CERN Large Hadron Collider*, JINST **3** (2009) S08003.
- [3] ATLAS Collaboration, *ATLAS Inner Detector Technical Design Report, vol. I*, CERN-LHCC-1997-016, CERN, Geneva, 1997.
- [4] ATLAS Collaboration, *The ATLAS Inner Detector commissioning and calibration*, Eur. Phys. J. **C70** (2010) 787 – 821, DOI: [10.1140/epjc/s10052-010-1366-7](https://doi.org/10.1140/epjc/s10052-010-1366-7).
- [5] ATLAS Collaboration, *ATLAS Data Quality Information*, <https://twiki.cern.ch/twiki/bin/view/AtlasPublic/RunStatsPublicResults2010>.
- [6] ATLAS Collaboration, *Study of alignment-related systematic effects on the ATLAS Inner Detector tracking*, <https://cds.cern.ch/record/1483518>, 2012. ATLAS-CONF-2012-141.
- [7] ATLAS Collaboration, *Measurement of the Muon Charge Asymmetry from W Bosons Produced in pp Collisions at  $\sqrt{s} = 7\ \text{TeV}$  with the ATLAS detector*, Phys. Lett. B **701** (2011) 31–49, arXiv:1103.2929 [hep-ex].
- [8] ATLAS Collaboration, *Characterization of Interaction-Point Beam Parameters Using the pp Event-Vertex Distribution Reconstructed in the ATLAS Detector at the LHC*, <https://cds.cern.ch/record/1277659>, 2010. ATLAS-CONF-2010-027.
- [9] ATLAS Collaboration, *Performance of primary vertex reconstruction in proton-proton collisions at  $\sqrt{s} = 7\ \text{TeV}$* , <http://cdsweb.cern.ch/record/1281344>, 2010. ATLAS-CONF-2010-069.
- [10] ATLAS Collaboration, *Performance of the ATLAS Secondary Vertex b-tagging Algorithm in 7 TeV Collision Data*, <http://cdsweb.cern.ch/record/1277682>, 2010. ATLAS-CONF-2010-042.
- [11] ATLAS Collaboration, *Performance of Impact Parameter-Based b-tagging Algorithms with the ATLAS detector using Proton-Proton Collisions at  $\sqrt{s} = 7\ \text{TeV}$* , <http://cdsweb.cern.ch/record/1299106>, 2010. ATLAS-CONF-2010-091.
- [12] ATLAS Collaboration, *Commissioning of the ATLAS high-performance b-tagging algorithms in the 7 TeV collision data*, [dunno](https://cds.cern.ch/record/1299106), 2011. ATLAS-CONF-2011-102.
- [13] ATLAS Collaboration, *Measurement of the  $B_d^0$  and  $B_s^0$  lifetimes in the decay modes  $B_d^0 \rightarrow J/\psi K^{*0}$  and  $B_s^0 \rightarrow J/\psi \phi$  in ATLAS*, <http://cdsweb.cern.ch/record/1369219>, 2011. ATLAS-CONF-2011-092.

- [14] ATLAS Collaboration, *Measurement of the average  $B$  lifetime in inclusive  $B \rightarrow J\psi X \rightarrow \mu^+\mu^-X$  decays with the ATLAS detector*, <http://cdsweb.cern.ch/record/1389455>, 2011. ATLAS-CONF-2011-145.
- [15] ATLAS Collaboration, *Measurement of the  $\Lambda_b$  lifetime and mass in the ATLAS experiment*, Phys. Rev. **D 87** (2013) 032002, [arXiv:1207.2284v3](https://arxiv.org/abs/1207.2284v3) [hep-ex].
- [16] ATLAS Collaboration, *Alignment Performance of the ATLAS Inner Detector Tracking System in 7 TeV proton-proton collisions at the LHC*, <http://cdsweb.cern.ch/record/1281342>, 2010. ATLAS-CONF-2010-067.
- [17] ATLAS Collaboration, *Alignment of the ATLAS Inner Detector Tracking System with 2010 LHC proton-proton collisions at  $\sqrt{s}=7$  TeV*, <https://cds.cern.ch/record/1334582>, 2011. ATLAS-CONF-2011-012.
- [18] P. F. Akesson *et al.*, *ATLAS Tracking Event Data Model*, <https://cds.cern.ch/record/973401>, 2006. ATL-SOFT-PUB-2006-004.
- [19] T. Cornelissen, *Track Fitting in the ATLAS Experiment*. PhD thesis, Universiteit van Amsterdam, 2006. CERN-THESIS-2006-072, <http://cds.cern.ch/record/1005181>.
- [20] ATLAS Collaboration, *Common Framework Implementation for the Track-Based Alignment of the ATLAS Detector*, <https://cds.cern.ch/record/1670354>, 2014. ATL-SOFT-PUB-2014-003.
- [21] P. Bruckman, A. Hicheur and S. Haywood, *Global  $\chi^2$  approach to the alignment of the ATLAS silicon tracking detectors*, <https://cds.cern.ch/record/835270>, 2005. ATL-INDET-PUB-2005-002.
- [22] A. Bocci and W. Hulsbergen, *TRT alignment for SR1 cosmics and beyond*, <https://cds.cern.ch/record/1039585>, 2007. ATL-INDET-PUB-2007-009.
- [23] A. K. Morley, *Electron Bremsstrahlung Studies and Track Based Alignment of the ATLAS Detector*. PhD thesis, The University of Melbourne, 2010.
- [24] A. Andreazza, V. Kostyukhin and R.J. Madras, *Survey of the ATLAS pixel detector components*, <https://cds.cern.ch/record/1097395>, 2008. ATL-INDET-PUB-2008-012.
- [25] T. Sjostrand, S. Mrenna, and P. Skands, *A brief introduction to PYTHIA 8.1*, Computer Physics Communications **178** (2008) no. 11, 852.
- [26] ATLAS Collaboration, *Muon reconstruction efficiency and momentum resolution of the ATLAS experiment in proton-proton collisions at  $\sqrt{s}=7$  TeV in 2010*, [arXiv:1404.4562](https://arxiv.org/abs/1404.4562) [hep-ex].
- [27] ATLAS Collaboration, *Public Pixel Plots for Collision Data*, <https://twiki.cern.ch/twiki/bin/view/AtlasPublic/PixelPublicResults>.
- [28] ATLAS Collaboration, *Public SCT Plots for Collision Data*, <https://twiki.cern.ch/twiki/bin/view/AtlasPublic/SCTPublicResults>.
- [29] M. Aleksa, F. Bergsma, P. A. Giudici, A. Kehrl, M. Losasso, X. Pons, H. Sandaker, P. S. Miyagawa, S. W. Snow, J. C. Hart, and L. Chevalier, *Measurement of the ATLAS solenoid magnetic field*, Journal of Instrumentation **3** (2008) no. 04, P04003.
- [30] K. Nakamura *et al.*, *Review of Particle Physics*, Journal of Physics G **37** (2010) .

- [31] ATLAS Collaboration, *Tracking Studies for  $b$ -tagging with 7 TeV Collision Data with the ATLAS Detector*, <https://cds.cern.ch/record/1281352>, 2010. ATLAS-CONF-2010-070.
- [32] ATLAS Collaboration, *A neural network clustering algorithm for the ATLAS silicon pixel detector*, arXiv:1406.7690 [hep-ex].

## A Detector Movements

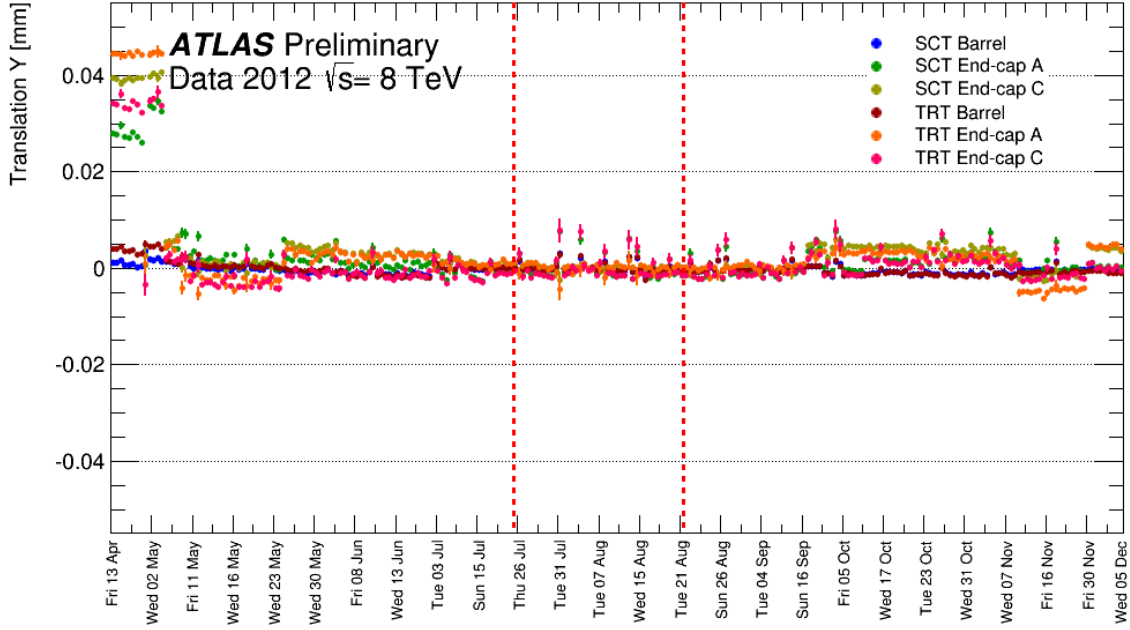


Figure 33: The corrections to the global  $Y$  position ( $T_y$ ) of all ID sub-detectors with respect to the pixel detector during 2012. The vertical dashed lines indicate the data-taking periods in which the baseline constants were determined. Errors show are statistical uncertainties on determined alignment parameter and crucially depend on the statistics of data recorded in a given run.

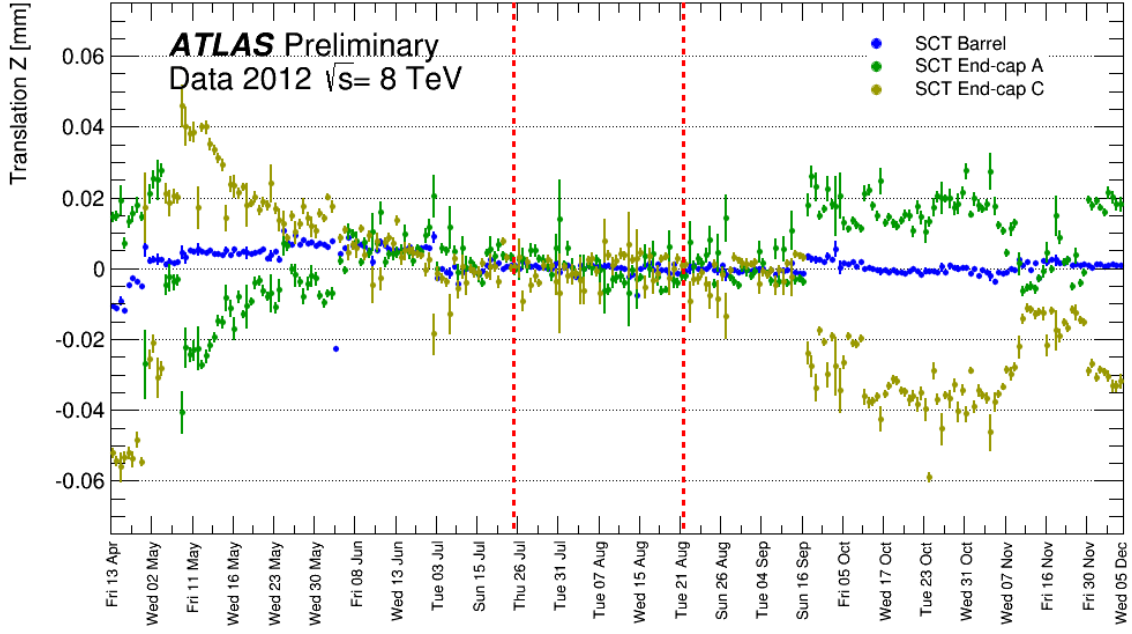


Figure 34: The corrections to the global Z position ( $T_z$ ) of all ID sub-detectors with respect to the pixel detector during 2012. The vertical dashed lines indicate the data-taking periods in which the baseline constants were determined. Errors show are statistical uncertainties on determined alignment parameter and crucially depend on the statistics of data recorded in a given run. TRT is not shown as it is not aligned in this DoF (see Table 2).

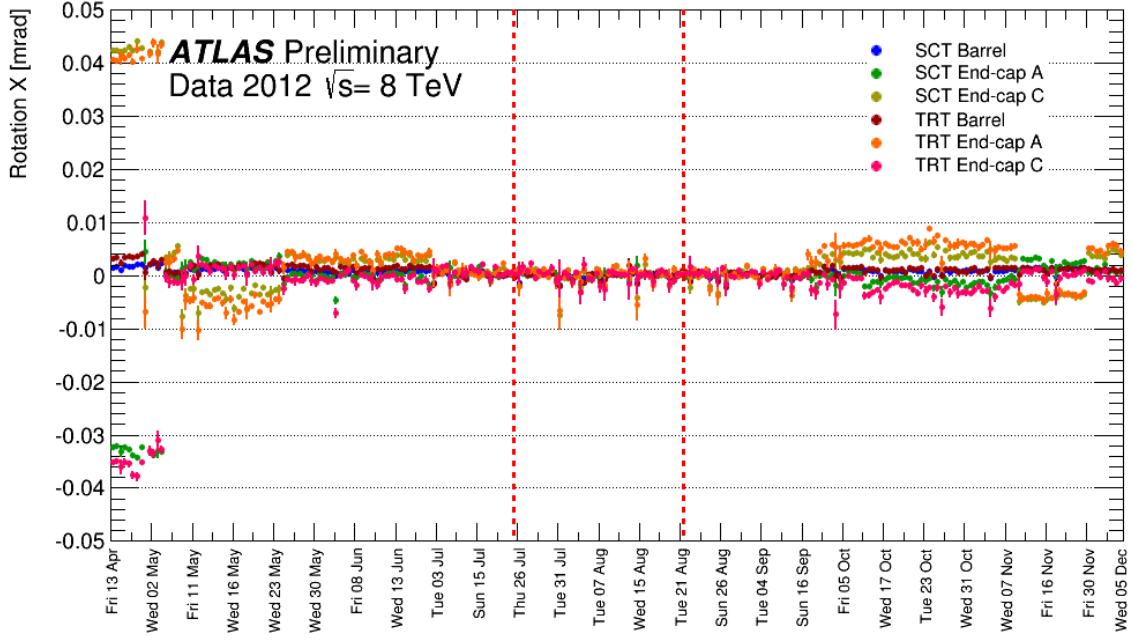


Figure 35: The corrections to the global X rotations ( $R_X$ ) of all ID sub-detectors with respect to the pixel detector during 2012. The vertical dashed lines indicate the data-taking periods in which the baseline constants were determined. Errors show are statistical uncertainties on determined alignment parameter and crucially depend on the statistics of data recorded in a given run.

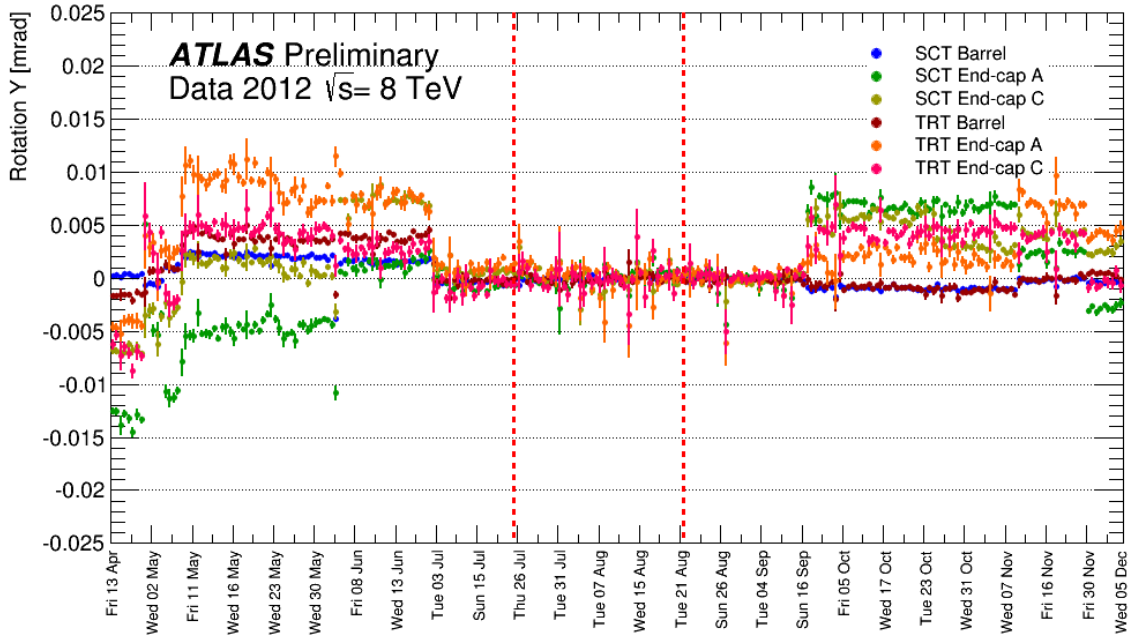


Figure 36: The corrections to the global Y rotations ( $R_Y$ ) of all ID sub-detectors with respect to the pixel detector during 2012. The vertical dashed lines indicate the data-taking periods in which the baseline constants were determined. Errors show are statistical uncertainties on determined alignment parameter and crucially depend on the statistics of data recorded in a given run.



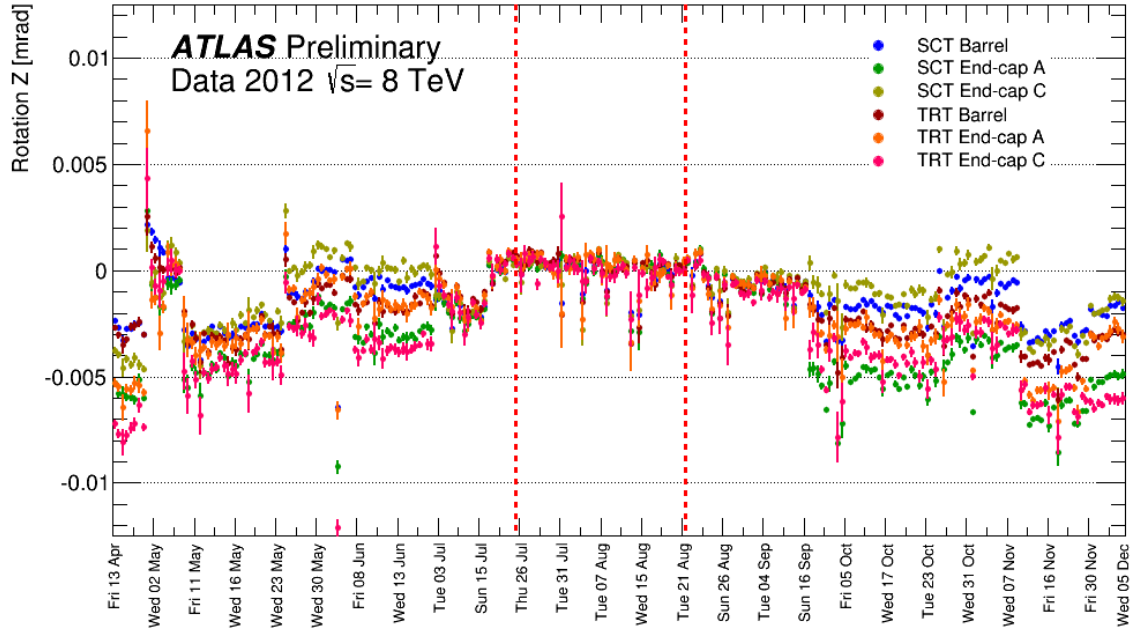


Figure 37: The corrections to the global Z rotations ( $R_z$ ) of all ID sub-detectors with respect to the pixel detector during 2012. The vertical dashed lines indicate the data-taking periods in which the baseline constants were determined. Errors show are statistical uncertainties on determined alignment parameter and crucially depend on the statistics of data recorded in a given run.